HHS Public Access

Author manuscript

Hear Res. Author manuscript; available in PMC 2018 February 01.

Published in final edited form as:

Hear Res. 2017 February ; 344: 207–222. doi:10.1016/j.heares.2016.11.018.

Multiscale Mapping of Frequency Sweep Rate in Mouse Auditory Cortex

John B. Issa[1,‡], **Benjamin D. Haeffele**[1], **Eric D. Young**[1,3], and **David T. Yue**[1,2,3]

[1]Department of Biomedical Engineering, The Johns Hopkins University School of Medicine, Ross Building, Room 713, 720 Rutland Avenue, Baltimore, MD 21205, USA

[2]Center for Cell Dynamics, The Johns Hopkins University School of Medicine, 720 Rutland Avenue, Baltimore, MD 21205, USA

[3]Solomon H. Snyder Department of Neuroscience, The Johns Hopkins University School of Medicine, 725 N. Wolfe Street, WBSB, Baltimore, MD 21205, USA

Abstract

Functional organization is a key feature of the neocortex that often guides studies of sensory processing, development, and plasticity. Tonotopy, which arises from the transduction properties of the cochlea, is the most widely studied organizational feature in auditory cortex; however, in order to process complex sounds, cortical regions are likely specialized for higher order features. Here, motivated by the prevalence of frequency modulations in mouse ultrasonic vocalizations and aided by the use of a multiscale imaging approach, we uncover a functional organization across the extent of auditory cortex for the rate of frequency modulated (FM) sweeps. In particular, using two-photon Ca^{2+} imaging of layer 2/3 neurons, we identify a tone-insensitive region at the border of AI and AAF. This central sweep region behaves fundamentally differently from nearby neurons in AI and AII, responding preferentially to fast FM sweeps but not to tones or bandlimited noise. Together these findings define a second dimension of organization in the mouse auditory cortex for sweep rate complementary to that of tone frequency.

Keywords

in vivo two-photon calcium imaging; auditory cortex; cortical organization; frequency modulated sweeps

[‡]To whom correspondence should be addressed: voice: (410) 955-0079, fax: (410) 955-0549, john.issa@gmail.com.

CONFLICT OF INTEREST

The authors declare no competing financial interests.

AUTHOR CONTRIBUTIONS

All authors conceived the project. J.B.I. and B.D.H. built the experimental setup and processed data. J.B.I. performed experiments, analyzed data, and wrote the paper. J.B.I., B.D.H., and E.D.Y. edited the paper. E.D.Y. and D.T.Y. supervised the project.

1. Introduction

Functional maps of sensory cortices have provided blueprints for key studies of cortical development and experience-dependent plasticity (Buonomano and Merzenich, 1998; de Villers-Sidani et al., 2008; Karmarkar and Dan, 2006). These maps often reflect the topology of the sensory organ. In auditory cortex, the parameter most commonly represented in these maps is the frequency of a pure tone, which arises from the mechanical transduction of sound waves in the inner ear (Moore, 1995; Von Békésy, 1960). The resulting spectral or tonotopic organization of the cochlea is mirrored throughout the auditory system (Hackett et al., 2011; Kaas, 2011). However, this narrowband representation is not enough for recognition of complex sounds. Rather, the auditory system must integrate across spectral and temporal dimensions to extract higher order features of sound. Such integration begins in subcortical areas (Clopton and Winfield, 1974; Covey and Casseday, 1999; Poon and Yu, 2000) but is refined via cortical processing (Zhang et al., 2003). The resulting functional specialization for various complex sound features (Chechik et al., 2006; Chi et al., 2005; King and Nelken, 2009; Rauschecker, 1998) has been observed in humans (Norman-Haignere et al., 2015) and non-human primates (Bendor and Wang, 2005; Rauschecker and Scott, 2009) but is not as well-understood in other animal models such as rodents (Linden et al., 2003).

Ethological factors play a key role in the nature of these organizational properties since auditory cortex is thought to develop based on the statistics of environmental sounds, especially those that carry behavioral relevance (Klug and Grothe, 2010; Singh and Theunissen, 2003). In mice, ultrasonic vocalizations used for communication contain complex acoustical features (Neunuebel et al., 2015). Frequency modulated (FM) sweeps are especially prevalent, appearing in the form of upward sweeps, downward sweeps, chevrons, and reverse chevrons (Grimsley et al., 2011; Holy and Guo, 2005; Portfors, 2007). More generally, frequency modulations are ubiquitous across species, present in the vocalizations of bats (Neuweiler, 1989), marmosets (Pistorio et al., 2006), macaques (May et al., 1989), and humans (Altmann and Gaese, 2014). Given this widespread behavioral relevance of FM sweeps, a specialization for processing of FM sweeps is predicted at the level of auditory cortex.

In fact, prior studies have pointed towards auditory cortex as critical for the discrimination of FM sweeps in many species including mice (Letzkus et al., 2011), rats (Rybalko et al., 2006), and Mongolian gerbils (Ohl et al., 1999). In bats, cortical circuits responsible for FM sweep processing, such as the FM-FM area involved in echolocation, have been implicated (Suga et al., 1983). In other species, certain regions prefer faster FM sweeps, such as a ventral region at the border of the primary auditory cortex (AI) and the secondary auditory cortex (AII) in cats (Mendelson et al., 1993), various lateral belt areas in rhesus monkeys (Tian and Rauschecker, 2004), and the anterior auditory field (AAF) in mice (Trujillo et al., 2011). In addition, regions of the ultrasonic field (UF) have been noted to prefer frequency modulations (Stiebler et al., 1997) and are selective for reversals in FM direction (Honma et al., 2013; Tsukano et al., 2016, 2015). While these studies highlight the potential specialization of cortical regions for FM sweep processing, a more comprehensive mapping of FM selectivity, which would facilitate the search for dedicated FM areas, is lacking.

Optical Ca^{2+} imaging opens the door for powerful studies on the functional architecture of cortical circuits by allowing for functional imaging with both large scale and single neuron resolution (Issa et al., 2014; Wekselblatt et al., 2016). In particular, a multiscale approach in transgenic mice provides for visualization of both global maps under widefield epifluorescence imaging and cellular-resolution maps under two-photon imaging in the same preparation. Here, we perform multiscale imaging in search of a functional organization for the rate of FM sweeps in the mouse auditory cortex. We find that tonotopic regions prefer slow-FM sweeps while fast-FM regions overlap with tone-insensitive regions in a manner that cannot be predicted from sensitivity to bandlimited noise. These global organizational features are consistent down to the single-neuron level, pointing towards a fine-scale organization of mouse auditory cortex for the processing of behaviorally-relevant complex features of sound.

2. Material and methods

2.1. Animal surgery

All animal procedures were approved by the Johns Hopkins Institutional Animal Care and Use Committee and have been described previously (Issa et al., 2014). Cre-dependent GCaMP3 mice (R26-lsl-GCaMP3, Ai38 from Jackson Labs, JAX no. 014538) (Zariwala et al., 2012) were crossed with Syn1-Cre mice (JAX no. 003966) (Zhu et al., 2001) or Emx1-Cre mice (JAX no. 005628) (Gorski et al., 2002), resulting in GCaMP3-Syn1 (Syn1-Cre; R26-lsl-GCaMP3) or GCaMP3-Emx1 (Emx1-Cre; R26-lsl-GCaMP3) mice to be used for imaging experiments. These transgenic mice allow for stable and widespread expression of GCaMP3 in neurons of the neocortex, thus facilitating functional imaging of neural activity. A total of 11 males and 7 females were used; all of the females were virgins. Under isoflurane anesthesia (1–2% in 0.5 L/min O_2), tissue overlying left auditory cortex was exposed and the skull was fixed with dental cement to a custom headpost. Body temperature was maintained near 37°C as measured by a rectal probe. Lidocaine (2%) with epinephrine (1:100,000) was applied locally for analgesia. Dexamethasone (~5 mg/kg, i.p.) was administered for inflammation and normal saline (0.5 ml, i.p.) for dehydration. The skull was thinned by a high speed drill (Foredom MH-170) and covered with either 0.9% saline or petroleum jelly to increase transparency. At this point the mouse was restrained and given a few minutes to recover from anesthesia before performing widefield transcranial imaging, after which the mouse was returned to 1% isoflurane and a 1–2 mm craniotomy performed. To dampen pulsations, the craniotomy was filled with 1.5–2% agarose (A9793, Sigma-Aldrich) and a glass coverslip affixed with dental cement. For a subset of experiments (138 of 920 active neurons in this study), immediately following the craniotomy AM ester of Fluo-2 MA (TEFLabs) at a final dye concentration of ~0.75 mM was pressure injected (10–50 kPa) via glass pipette 200–300 μm below dura under two-photon imaging guidance. Fluo-2 provided brighter signal but was extruded from cells within 2–3 hours, so for the majority of experiments we relied on GCaMP3 fluorescence. After waiting at least 10 minutes post-anesthesia, two-photon imaging was performed on unanesthetized restrained mice with the head rotated ~45° about the coronal axis to bring the surface of left auditory cortex perpendicular to the microscope objective.

For a subset of experiments, GP4.12 *Thy1*-GCaMP6s mice (Dana et al., 2014, p. 1) were implanted with chronic windows. Surgical procedures were identical to those described above for acute windows except that instruments were sterilized by autoclave and mice were given carprofen (5 mg/kg, s.c.) perioperatively for inflammation and buprenorphine (0.5 mg/kg, i.p.) postoperatively for pain. After 7–10 days, mice were habituated to head-fixation while running on a ball before imaging sessions began. Imaging habituated mice on the ball appeared to minimize both discomfort for the mice and motion artifacts of the imaging field. While running has been shown to suppress auditory cortical activity (Schneider et al., 2014), for the purposes of this study we did not examine the influence of running behavior on cortical responsiveness.

2.2. Imaging

Widefield imaging was performed using a GFP filter cube (460/50 excitation, 540/50 emission) and a white light source (X-cite 120Q or LED Engin LZ1-10CW00). GCaMP3 fluorescence was collected through a 10× 0.25 NA objective (Olympus) by a Photometrics CoolSnap HQ camera, furnishing a 2×2 mm^2 field of view with a pixel size of 15×15 μm^2. Illumination power density was 0.25 mW/mm^2. For GCaMP6s, a Photometrics Evolve 512 camera was used instead.

Two-photon Ca^{2+} imaging was performed using an Ultima system (Prairie Technologies) with a mode-locked laser (Coherent Chameleon XR Ti:Sapphire) tuned to 950 nm and raster scanned at 5–12 Hz via a pair of galvanometer mirrors. Laser power at the sample was between 20–80 mW. Typically a 40× 0.8 NA objective (Olympus) was used, although in some instances a 25× 1.05 NA objective (Olympus XLPlan N) was used. Resolution along the *y*-axis was reduced by a factor of 4× for faster imaging, yielding a final pixel size of 0.45×1.8 μm (or 0.7×2.9 μm with the 25× objective). Dwell time was either 2 or 4 μs. Green emission channel (525/70 nm) was used for GCaMP3 or Fluo-2 fluorescence. Cells were imaged at depths of 150 to 430 μm, with the majority (73%) between 200 and 300 μm.

2.3. Auditory stimulation

The imaging set-up was located within a sound-treated room (Acoustical Solutions, Inc., AudioSeal ABSC-25). Ambient noise levels were measured using both a Bruel & Kjær ¼” type 4939 microphone and a probe tube designed by G. Sokolich, which has a useful frequency response up to 100 kHz. With both instruments, noise was found to be below the threshold for mouse hearing, with spectrum levels over a 1 Hz band (dB *re*: 20 $\mu Pa/Hz^{½}$) of −10 dB or less. These calibrations have been previously published (Issa et al., 2014, Figure S4).

Sounds were delivered by a free-field speaker (Tucker-Davis Technologies, ES1) located 12 cm from the contralateral (right) ear. Using the two microphones mentioned above, intensity levels were flat within 15 dB between 3 to 96 kHz (Figure 1C, left). Total harmonic distortions were measured during frequency sweeps and found to be in the range of −30 to −40 dB for 3 to 96 kHz (Figure 1C, right). All stimuli were cosine-squared gated (1–5 msec) and played in random order with 1.5–2.5 sec between onsets. The short gate times were a compromise for the fastest FM sweeps and added ~2 kHz of spectral splatter that, if

anything, would make them more similar to bandlimited noise stimuli, especially at low frequencies. A single presentation of each stimulus was sufficient for transcranial imaging (although multiple trials were often run) while 3–10 repetitions were used for two-photon imaging. Stimuli were often presented at multiple levels, typically between −60 to −20 dB attenuation (~30 to 70 dB SPL using our speaker).

Acoustic stimuli are illustrated in Figure 1. Sinusoidal amplitude modulated (SAM) tones were 300 msec with a 10 Hz modulation. For transcranial imaging, 16 frequencies (which refers to the carrier frequencies) over 5 octaves (3 to 96 kHz) were used (3 frequencies per octave), while for two-photon imaging 30 frequencies over 4 octaves were used (7.25 frequencies per octave). Frequency modulated (FM) sweeps logarithmically swept a 5-octave frequency range (Nelken and Versnel, 2000) either upward (3 to 96 kHz) or downward (96 to 3 kHz) with durations that varied from 7.5 msec to 600 msec. Logarithmic FM sweeps were utilized because linear FM sweeps would disproportionately deliver energy in high-frequency spectral bands given the large frequency range covered. The large 5-octave range was used so that responses would not be biased towards the frequency tuning of any neuron. For transcranial mapping, 16 different sweep stimuli were used while for two-photon imaging 20 different sweep stimuli were used. Piecewise sweeps (PWS) were fixed at a given sweep rate and octave range (0.5 or 1 octaves) but varied in center frequency (4 to 64 kHz) and direction. As individual piecewise sweeps covered a much narrower frequency range than the full FM sweeps, they provided an important control for inhibition by frequencies outside the excitatory band. Bandlimited noise (BLN) were generated by bandpass filtering 300-msec of Gaussian noise with an FIR filter (using fir2 in MATLAB) and applying a 10 Hz amplitude modulation. Bandwidths were either 0.5, 1, or 2 octaves and, in some cases, stimuli with a 0.25-octave bandwidth were additionally used. Center frequencies ranged from 4 to 64 kHz, but for bandwidths of 1-octave or greater this range was reduced to 6–44 kHz or 6–48 kHz. Note that, since stimulus amplitudes were normalized relative to RMS, the average energy in a given frequency band decreased as the filter bandwidth was increased. Thus, in going from 0.5 to 2 octaves, sound intensity decreased by ~6 dB/$Hz^{½}$.

2.4. Data analysis

Four categories of data analysis were carried out: transcranial image analysis, two-photon image analysis, registration, and response metrics. The majority of these methods have been described previously in detail (Issa et al., 2014).

For transcranial imaging, each frame of the fluorescence time series was normalized by a spatially low-pass filtered version of the mean intensity image. Next a structured sparse encoding algorithm was employed to detect the baseline and denoise the data (Haeffele et al., 2014). Finally, responses were deblurred with a Lucy-Richardson deconvolution using a Gaussian with a 200-μm width as the point spread function (Lucy, 1974; Richardson, 1972).

For two-photon imaging, cells were manually circled to delineate regions-of-interest (ROIs) and generate brightness-over-times (BOTs) for each cell. Cell identification was initially based on structural features, such as nuclear exclusion of GCaMP fluorescence with somas ~10 μm in size (Tian et al., 2009). However, as many cells are not visible when silent, we

then selected cells based on functional features by looking for spatially-consistent transients present in any of the trials for a given field-of-view, i.e. for somas that blinked on and off with activity. This initial selection of cells was aggressive so that there would not be a bias towards the most active cells. For each trial (40–60 s in duration), $\Delta F/F_O$ was calculated, where the baseline F_O was found by removing any points more than 1.5 standard deviations above the mean and then iterating until all remaining points were within 1.5 standard deviations.

For further analysis, only cells that showed at least one transient during an imaging session were included. Transients had to be larger in magnitude than the corresponding neuropil signal, which helped limit the influence of neuropil contamination on our signals. We also performed all analysis on neuropil-subtracted data by subtracting 0.7 times the neuropil signal from individual BOTs, where the neuropil signal was taken as the average signal of all image pixels outside of cellular ROIs (Chen et al., 2013). The fraction of responsive neurons fell from 48.5% to 38.4% following neuropil correction but statistical tests used in this study were not significantly altered; results after neuropil subtraction are stated where appropriate. A non-negative deconvolution method was applied to generate spike probabilities (Vogelstein et al., 2010), which were then thresholded to estimate events per time bin, where events serve as a proxy for action potentials (Smetters et al., 1999). Such an approach has been validated *in vivo* and applied to GCaMP signals in different regions of mouse cortex (Bonin et al., 2011; Froudarakis et al., 2014; Hofer et al., 2011; Ko et al., 2011; Petreanu et al., 2012; Rajasethupathy et al., 2015). This statistic (events per time bin) was used for subsequent analysis.

2.5. Registration

Registration was performed by aligning vasculature landmarks from widefield imaging with those from two-photon imaging (achieved by focusing up to the dura). For registration of fields of view (FOVs) across animals, we used a landmark-based radial-basis function (RBF) method to perform a local elastic registration (Arad and Reisfeld, 1995; Cavoretto et al., 2011). The landmarks used were the 3 ‘L’ and 4 ‘H’ fiduciaries derived from the centers-of-mass of regions that responded most strongly to low- and high-frequency tones, respectively (Figure 2C). The details of this registration have been described previously (Issa et al., 2014).

2.6. Response metrics

Response for any given stimulus was calculated as the integral of the baseline-corrected deconvolved signal over the first 600 msec after the start of each stimulus, which was then normalized as event rate by dividing by 600 msec. While stimuli varied drastically in their durations, we chose to use this fixed 600 msec window across all stimuli because our frame rates (typically < 10 Hz) precluded a high level of temporal precision. Frames with excessive motion artifacts were excluded from these calculations.

For transcranial imaging, the preferred frequency at each pixel location was calculated as the weighted average of the three frequencies eliciting the largest responses. For two-photon imaging, a significant response to any given stimulus condition was defined as the evoked

activity of the neuron surpassing baseline by at least 1 standard deviation plus an average of 5 events per second. Best frequency was calculated at threshold, defined as the lowest sound level eliciting a significant response at one or more frequencies, and taken as the median value of three different measures: 1) the mean of a least-squares fitted Gaussian, 2) the weighted average of all significant responses, and 3) the frequency eliciting the maximum response. This approach allowed approximation of the best frequency in cases where more than one frequency elicited a response at the lowest sound level tested. Population FRAs for a given field are the average firing rate (events per second) of all active neurons. Best sweep rate was calculated using an identical procedure to best frequency but with sweep rate as the variable of interest and with responses to up and down FM sweeps combined.

The direction selectivity index (DSI) was calculated as $(r_{up}-r_{down})/(r_{up}+r_{down})$, where r_{up} and r_{down} are the mean responses to upward and downward sweeps, respectively (Trujillo et al., 2011). To attain a measure of the statistical significance of direction selectivity, 2-way ANOVA was calculated for responses to FM sweeps with sweep rate and direction as the variables, and $p < 0.1$ was the criteria for a significant direction selectivity. Note that this criteria was sensitive to differences in sweep rate tuning for different directions. For example, a neuron that differed in its sweep rate tuning for upward and downward sweeps, even if the total response to upward and downward sweeps was identical, would be classified as direction selective by our criteria.

Maximal responsiveness within a particular stimulus class was taken as the maximal driven rate above baseline in events per second for a given stimulus paradigm within that stimulus class. For example, if BLN of two different bandwidths were tested at three different sound levels, a driven rate would be calculated for that neuron for the 6 different bandwidth-level combinations, and the maximum of those values would be used as the maximal responsiveness of that neuron for BLN. These values were used to classify neurons based on which stimulus class elicited the largest ‘maximal responsiveness’ for that neuron among the four stimulus classes shown in Figures 1 and 10A. Only neurons with a significant response to at least one stimulus were included (152 of 307 neurons).

3. Results

3.1. Mapping FM sweep responses via widefield imaging

We performed widefield epifluorescence imaging of auditory cortex in unanesthetized mice expressing GCaMP3 in neurons while SAM tones were played to the contralateral ear. Examples of responses in three neighboring cortical regions are shown in Figure 2A to emphasize spatial variation in responses. Region 1 was tuned preferentially to high frequency tones while region 2 preferred low frequency tones (Figure 2B). Region 3, however, was comparatively unresponsive to tones of any frequency. This trend was further validated by considering spatial response maps across the entire imaging field. As observed previously (Issa et al., 2014), low frequency SAM tones induced responses in three spatially distinct regions or poles, labeled ‘L’ (Figure 2C, left), while high frequency tones drove responses in four poles, labeled ‘H’ (Figure 2C, right). The average strength of response across all 16 frequencies of SAM tones (which we refer to as the average response map) highlights strongly tone-responsive regions along tonotopic axes connecting ‘L’ and ‘H’

poles in AI, AAF, and AII. A tone-insensitive region (darker areas encircled by red oval) was observed at the presumptive border of AI and AAF (Figure 2D), consistent with the low level of tone responses observed in region 3.

As other sounds may excite the tone-insensitive regions shown in Figure 2D, we tested a set of FM sweeps that logarithmically span 5 octaves, from 3 to 96 kHz, in order to cover the entire range of mouse hearing (Taberner and Liberman, 2005), while varying the direction (ascending or descending in frequency) and sweep rate (from 8 to 670 oct/s) of each stimulus. Signals displayed in Figure 2E correspond to the three regions marked in Figure 2A, and the affiliated sweep rate and direction for each stimulus presentation are marked on the axis below. Region 1 was weakly responsive with a preference for the slowest FM sweeps while region 2 responded strongly with a preference for slow FM sweeps. Region 3, which was indifferent to SAM tones, responded robustly to fast FM sweeps. Spatial response maps for responses to individual FM sweeps of different rates and directions are shown in Figures 2F and 4A. The slow sweep (at 8 oct/s) elicited responses in three distinct regions, marked as slow poles (‘S’, Figure 2F, left), while the fast sweep (at 356 oct/s) elicited responses in three regions as well, now marked as fast poles (‘F’, Figure 2F, right). Results for upward and downward FM sweeps were similar (Figure 2F, top versus bottom) and highly correlated on a pixel-by-pixel basis (Figure 3A–C; $\rho = 0.99$ via Spearman correlation for single experiment shown and 0.99 ± 0.01 across eight experiments; null distribution estimate of Spearman correlation based on resampling SAM tone responses was 0.96 ± 0.03). Thus the same ‘S’ and ‘F’ poles were used as landmarks for both sweep directions. Responses across all 8 FM sweep rates were then averaged, and slow and fast poles were displayed on the same map to highlight differences in their locations (Figure 2G). Of particular note, sweeps elicited large responses in some regions that were not appreciably responsive to SAM tones (e.g. in the ventral part of the red oval).

Next we asked whether the strength of response to SAM tones may be correlated with tuning for FM sweep rate. Response patterns for the two slowest FM sweep rates used (8 and 16 oct/s) resembled those for SAM tones (compare Figure 2D to middle panel of Figure 3D), while the response patterns for the fastest FM sweep rates used (360 and 670 oct/s, left panel of Figure 3D) differed markedly, highlighted by taking the difference in response strength for fast versus slow FM sweeps (Figure 3E). To quantify these correlations, scatter plots of response strength for slow FM sweeps versus SAM tones and fast FM sweeps versus SAM tones (Figure 3F) for each pixel were plotted, confirming a much higher degree of correlation between responses to slow FM sweeps and SAM tones (Figure 2H and Figure 3F; $\rho = 0.72$ via Spearman correlation for single experiment and 0.80 ± 0.06 across eight experiments; again, null distribution estimate was 0.96 ± 0.03).

Spatial maps of spectral tuning were then formed by calculating a best frequency at each pixel in the image across all 16 tone frequencies tested; for spatial maps of sweep rate tuning, best sweep rate was calculated across all 8 sweep rates tested (Figure 4A–D). Fast-FM regions, indicated by red, clustered around ‘F’ poles while slow-FM regions, indicated by blue, dominated in regions surrounding the tonotopic gradients connecting ‘L’ and ‘H’ poles as in Figure 2D. To determine whether any gradients exist in sweep rate tuning, we tracked local centers-of-mass across all sweep rates (cyan and magenta dots, Figure 4A). We

demonstrated three gradients, superimposed as thick cyan and magenta traces for up and down sweep responses, respectively (Figure 4B). The magenta trace is largely obscured by the cyan trace, indicating that the sweep-rate gradients are independent of sweep direction. Transcranial sweep-rate maps were similar across mice (Figure 4E), with a consistent layout of sweep-rate-preferring regions relative to observed tonotopic gradients. A canonical map, formed by merging eight individual maps after a landmark-based registration (see Methods), resembled maps from individual mice (Figure 4F). We restricted this averaging to mice with minimal motion artifacts during widefield imaging. Of note, we used the set of landmarks derived from SAM tone responses (L and H poles) to register the FM sweep maps. Across eight experiments, the layout of slow and fast FM sweep centers (taken as the centers of mass of responses to the slowest and fastest FM sweeps) is shown in Figure 4H along with the average length of all tone frequency and FM sweep rate gradients. This registration substantiates the reproducibility of maps across mice and the relative layout of tone and sweep responses.

To test whether these results were dependent on the sensitivity of the Ca^{2+} indicator used or on the state of the animal, a chronic window was placed over auditory cortex in a transgenic mouse expressing GCaMP6s (*GP4.12 Thy1-GCaMP6s*) (Dana et al., 2014, p. 1). GCaMP6s is an ultrasensitive indicator with rise and decay kinetics roughly threefold slower than GCaMP3 (Chen et al., 2013). Unlike previous mice, which were fully restrained and imaged on the same day as receiving anesthesia for attachment of a head post, this mouse was imaged three weeks after implantation of the window. The SAM tone and FM sweep maps were structurally similar between this mouse and the GCaMP3 mice as shown in Figure 4G, and the length of gradients displayed a similar pattern as well, as indicated by the open circles in Figure 4H. For this mouse, responses between SAM tones and slow FM sweeps were highly similar ($r = 0.95$ via Pearson's analysis) while those between SAM tones and fast FM sweeps were not ($r = 0.44$), in agreement with the results from mice expressing GCaMP3.

3.2. FM selectivity differs for single neurons in three distinct regions

Based on these widefield imaging results, a working model of cortical organization is represented in Figure 4I, illustrating the relationship between named tonotopic regions (AI, AII, and AAF) and fast-sweep rate regions. To explore whether this organization holds true at the level of individual neurons, we performed two-photon Ca^{2+} imaging, focusing on three regions that exhibited distinct response profiles by widefield imaging: AI, AII, and a third region located along dorsal AII at the border of AI and AAF. For convenience, we will refer to this border region as the central sweep region (CSR) throughout this study. AI had demonstrated strong responses to tones, AII was responsive to both tones and FM sweeps, and CSR strongly preferred fast FM sweeps. Shown in Figure 5 are exemplar fields of view (FOVs) located in each of these regions.

The first field was located near the low-frequency pole of AI, determined by registering vasculature landmarks seen under widefield imaging with dura overlying our FOV seen via two-photon imaging (Figure 5A, left). Three exemplar neurons in this field, their locations highlighted in the right panel of Figure 5A, responded robustly to low frequency SAM tones

at −20 dB attenuation (Figure 5B, left). Frequency response areas (FRAs), formed from deconvolved and thresholded signals, summarize responses across all frequencies (*x*-axis) and sound levels (*y*-axis) tested. As shown in Figure 5B, right, all neurons were sharply tuned to low frequencies while response strength monotonically increased with sound level. By contrast, in response to FM sweeps, these same neurons were at best weakly responsive, with tuning for slow sweeps and a slight preference for upward sweeps (Figure 5C, left). Analogous to an FRA, we formed a sweep rate response area (SRA), which summarizes responses to all sweep rates and sound attenuations tested. Within each SRA thumbnail, responses to upward sweeps are shown on the left and those to downward sweeps on the right (Figure 5C, right). Again, these neurons responded weakly to FM sweeps but with a preference for slow upward sweeps at the loudest sound levels. The average FRA for this field demonstrates low frequency tuning while the average SRA demonstrates tuning for slow upward sweeps (Figure 5D). We formed a cumulative histogram of the maximal responsiveness to SAM tones and FM sweeps across attenuation levels, calculated as the total increase over baseline firing (Figure 5E). The responses to SAM tones were found to be significantly larger for this population ($p < 1e\text{-}4$, 2-sided Wilcoxon signed-rank test of 25 neurons). Across this entire field, 80% of active neurons were responsive to SAM tones while only 12% were responsive to FM sweeps.

Next we examined a two-photon imaging field in the central portion of AII (Figure 5F–J). This region possesses a weak tonotopic organization (Issa et al., 2014; Tsukano et al., 2015) and, based on our widefield imaging results (Figure 2D and 2G), should be strongly responsive to FM sweeps as well. Indeed, neurons in this field are tuned to high frequencies (Figure 5G) and, more interestingly, respond heterogeneously to sweep rate (Figure 5H). For example, neurons 4 and 5 prefer slow sweep speeds while neuron 6 is tuned to moderately fast sweeps in a bandpass manner. The population data for this field adheres to these trends (Figure 5I–J). Of the 42 active neurons in this field, 43% responded to SAM tones and 38% to sweeps, while the overall strength of responses to SAM tones was now slightly less than it was for FM sweeps (Figure 5J).

The final field was situated at the dorsal end of AII, approaching the border of AI and AAF, in what we term CSR (Figure 5K). Under widefield imaging, this region of cortex did not respond strongly to SAM tones but did prefer moderate-to-fast FM sweeps. Indeed, individual neurons in this field behaved drastically differently from those in the previous two regions. Neuron 7, for example, was unresponsive to SAM tones (Figure 5L, top) but responded robustly to medium-rate FM sweeps (Figure 5M, top). Moreover, this neuron was strongly direction selective ($p < 1e\text{-}9$, 2-way ANOVA). Neuron 8 was broadly tuned to SAM tones (Figure 5L, middle) and to FM sweeps (Figure 5M, middle) but was not direction selective ($p = 0.20$, 2-way ANOVA). Across the population of 40 active neurons, FM sweep responses were significantly stronger than SAM tone responses (Figure 5N–O; $p < 1e\text{-}5$, 2-sided Wilcoxon signed-rank test), with 18% of neurons responding to SAM tones and 38% responding to FM sweeps. Together, these results exhibit stark regional differences in the tuning of individual neurons for SAM tones and FM sweeps that echo the results observed under widefield imaging.

3.3. Population activity confirms functional differences between cortical regions

To confirm these trends on the population level, we combined data across 32 individual FOVs from 18 different mice imaged at depths ranging from 150 to 430 μm. Imaging was targeted to fields along the tonotopic axes of AI and AII and also in regions dorsal to AII. Individual fields and neurons were registered to the global map via a landmark-based elastic registration method (see Methods) and segmented into AI, AII, CSR, or 'other' based on Cartesian distance to L and H landmarks, resulting to the boundaries indicated in Figure 7. Table 1 and Figures 6 and 7 summarize the results. As in the exemplars shown in Figure 5, AI was more strongly responsive to SAM tones across the entire population (Figure 6A; $p <$ 1e-7, 2-sided Wilcoxon signed-rank test). AII was equally responsive to both classes of stimuli (Figure 6B; $p > 0.04$, 2-sided Wilcoxon signed-rank test). CSR was more strongly responsive to FM sweeps (Figure 6C; $p <$ 1e-7, 2-sided Wilcoxon signed-rank test). Sound-responsive neurons were then assigned to one of three categories—tone only, tone + sweep, and sweep only—based on whether they had a significant response to tones or sweeps (see Methods) and plotted on a schematized version of auditory cortex (Figure 7A). Tone-only neurons tended to reside in AI (Figure 7A, left) while sweep-only neurons clustered in CSR (Figure 7A, right). These trends are further substantiated in Table 1, which shows that sound-responsive AI neurons were most likely to be responsive only to SAM tones (64% of 143 neurons) while sound-responsive CSR neurons were most likely to be responsive only to FM sweeps (62% of 71 neurons). AII neurons showed a mixed distribution with almost equal numbers of neurons in all three categories. While 85% of our neurons were imaged in superficial layers (<350 μm), we tested for the possibility that these results were influenced by imaging depth and found no correlation in the preference for FM sweeps versus tones as a function of depth ($r = 0.11$ via Pearson's analysis).

Next we plotted the best frequency of all SAM tone responsive neurons (Figure 7B) and the best sweep rate of all FM sweep responsive neurons (Figure 7C). The color of each square encodes the preferred frequency (blue = low, red = high) or sweep rate (blue = slow, red = fast) of each neuron. As shown previously (Issa et al., 2014), tonotopic organization can be readily appreciated from the two-photon data across large regions, as Figure 7B demonstrates clustering of low frequency neurons (in blue) near the low-frequency poles of AI and AII and high-frequency neurons (in red) near the high-frequency poles of AI and AII. Figure 7C, which shows the distribution of regions in auditory cortex that preferred either slow or fast sweeps, matches with the widefield map shown in Figure 4D, except that no two-photon imaging fields were localized in the ventro-caudal part of AII, identified as a fast-sweep area in widefield imaging. As expected, neurons in AI and in the core of AII (along the central tonotopic gradient) tended to prefer slow sweeps, indicated by blue and cyan squares, while neurons in CSR along the AI-AAF border tended to prefer faster sweeps, indicated by orange and red squares. Histograms of sweep rate preference confirm these trends, as AI neurons tended to prefer the slowest sweep rates, with an average preferred rate of 20 oct/s (Figure 6D, left), while CSR had an average preferred rate of 84 oct/s (Figure 6D, right). AII was intermediate with a preferred rate of 52 oct/s and a fairly flat distribution across all sweep rates tested (Figure 6D, middle). The sweep rate preferences of both AII and CSR were significantly faster than for AI ($p <$ 1e-4, 2-tailed

Mann-Whitney). CSR and AII did not significantly differ from each other ($p = 0.093$, 2-tailed Mann-Whitney).

We also measured the correlation between responses to FM sweeps and responses to SAM tones as a function of sweep rate. This approach is analogous to the analysis performed for transcranial responses in Figure 3F–G, where responses to SAM tones correlated most strongly with responses to slow FM sweeps. Likewise, for individual neurons in all three regions, we found a strong correlation between responses to slow FM sweeps and SAM tones that decreased as the sweep rate was increased (Figure 6E).

We then computed the direction selectivity index (DSI) of each neuron that responded to FM sweeps (see Methods). Neurons were plotted on a single map, with red indicating neurons preferring downward sweeps and blue indicating neurons preferring upward sweeps (Figure 7D). Among neurons responsive to FM sweeps, neurons in AI were more likely to be direction selective (Table 1). But, similar to the widefield imaging results (Figure 3A–C), direction selectivity was not significantly different across cortical regions ($p > 0.1$ for all pairwise comparisons between regions, 2-tailed Mann-Whitney). DSI did depend on BF, however, as neurons with BFs below 12 kHz tended to have more positive DSIs than neurons with BFs above 12 kHz (0.284 versus −0.093; $p < 1e\text{-}7$, 2-sided Mann-Whitney), which is similar to prior work in rat AI (Orduña et al., 2001; Zhang et al., 2003).

3.4. Neurons in CSR are uniquely selective for FM sweeps

While neurons with a significant DSI can be considered truly sweep selective, roughly half of our sweep-responsive neurons were not direction-selective (out of 88 sweep-only and 89 sweep-and-tone responsive neurons, 87 were direction selective; Table 1). For these neurons, FM sweep responses could instead reflect tuning for broad-spectrum sounds as fast FM sweeps mimic the spectral content of broadband noise pulses. For example, neurons in cat AI tuned to fast FM sweeps also preferred broadband noise stimuli (Mendelson et al., 1993). Another possibility is that, as duration and sweep speed are confounded in our FM sweep stimuli (faster sweeps have shorter durations), a speed-selective neuron may primarily be duration selective. To explore these possibilities, we utilized two additional classes of stimuli: piecewise sweeps (PWS) and bandlimited noise (BLN). PWS consisted of FM sweeps with a fixed duration and sweep rate (chosen to span 0.5 or 1 octaves in frequency) but varied center frequency. BLN consisted of white noise filtered at a fixed octave range but with differing center frequencies. Thus both PWS and BLN were band-limited and center frequencies were changed to cover the entire frequency range (Figure 8A). Taking a reductionist approach, we hypothesize that neurons reside in a 2-dimensional response space (Figure 8B), where the FM-DC axis refers to preferences for frequency modulations or static components (here DC or ‘direct current’ refers to a constant frequency) and the tone-noise axis refers to preferences for SAM tones or broadband noise. Depending on where neurons fall in this space, they may be categorized into a number of response types, as shown in Figure 8C. Under this framework, we asked whether sweep-responsive neurons were bandwidth selective or truly rate selective.

First we examined responses to BLN under transcranial widefield imaging as we had done for SAM tones and FM sweeps in Figure 2. Stimuli consisted of ten noise bursts passed

through a 2-octave bandpass filter with center frequencies ranging from 6 to 48 kHz. The average response across these noise stimuli, shown in Figure 8D, was similar to the average response to SAM tones shown previously in Figure 2D. Strong responses are seen along the tonotopic axes of AI, AII, and AAF, with a dark central region along the border of AI and AAF. To facilitate comparison across stimulus classes, we took the difference between the average responses to BLN, SAM tones, and FM sweeps (Figure 8E). Again, responses to BLN and SAM tones were similar, with a slight preference for SAM tones along the tonotopic center of AII (Figure 8E, left). In contrast, FM sweeps differed significantly from both BLN (Figure 8E, middle) and SAM tones (Figure 8E, right), with similar patterns for both. Sweep regions illustrated in Figure 4I favored FM sweeps not just over SAM tones but over BLN as well, implying that the observed FM sweep selectivity is not a response simply to the broadband nature of the sweep.

To study these relationships at the single-neuron level, we utilized all four classes of stimuli in a subset of two-photon imaging experiments. Tuning curves for four neurons located at the border of CSR and AII are shown in Figure 8F–G. The stimulus set consisted of SAM tones, BLN at 0.25 octaves and 1 octave, PWS at 10 oct/s, and FM sweeps. Based on their response profiles, neuron 1 acted as a frequency filter, neuron 2 was rate selective, and neuron 3 appeared to be broadband selective. Neuron 4 was more complex, responding to both SAM tones and FM sweeps while being unresponsive to BLN. Tuning curves for another eight neurons from a different field at the border of AI and CSR are shown in Figure 9. In both cases, neurons responding to FM sweeps tended to respond to PWS but not to BLN, while neurons responding to BLN were not responsive to FM sweeps, except in the case of neurons that had responded well to SAM tones (neuron 1 of Figure 8F–G).

We examined these trends across 307 neurons for which all four classes of stimuli were tested. To analyze whether responses to BLN may predict responses to FM sweeps, we calculated the correlation coefficient between response strengths for each stimulus class, shown as bar plots in Figure 10A. Only the 152 neurons responsive to at least one stimulus class were included. FM sweep responses and BLN responses were not correlated ($r = -0.01$, $p > 0.1$ via Pearson's analysis), which contrasts with the high correlation observed between FM sweep responses and both SAM tone ($r = 0.39$, $p < 1e\text{-}6$) and PWS ($r = 0.72$, $p < 1e\text{-}9$) responses. These results indicate that responses to FM sweeps do not arise from a simple spectral integration over short time periods but rather likely involve processing of temporal dynamics in tone frequency. To examine whether responses were organized by cortical location, neurons with a significant response to at least one sound were categorized as SAM, BLN, PWS, or FM based on which of the four stimulus classes produced the largest maximal responsiveness in that neuron. Neurons belonging to each category were then plotted on a single map (Figure 10B). Neurons in AI were most likely to be driven by SAM tones or BLN while neurons in AII and CSR preferred FM sweeps and PWS (Figure 10C). Overall these results demonstrate that neurons driven by FM sweeps are driven by PWS but not BLN and that such neurons tend to reside in AII and CSR rather than AI.

4. Discussion

Our results uncover a functional organization for the rate of FM sweeps in the mouse auditory cortex. Whereas past approaches to mapping have had to sacrifice either cellular resolution, as is the case for intrinsic imaging methods, or scalability, as is the case for microelectrode recordings, this present study moves towards comprehensive brain mapping by taking advantage of transgenic GCaMP mice and multiscale imaging. We find that fast FM sweeps drive responses in regions of cortex not responsive to tones, thus adding a dimension of sweep-rate organization complementary to that of tonotopic organization.

While overall our tonotopic maps are similar to those of previous investigators (Guo et al., 2012; Hackett et al., 2011; Stiebler et al., 1997), there remains uncertainty about the tonotopic axis and strength of tone responses in AAF. In contrast to prior studies, we find little evidence for a dorsal low-to-high frequency gradient in AAF leading to the ultrasonic field (marked UF in Figure 2D) and instead observe a strong high-frequency region in ventral AAF. Moreover, we find that caudal and dorsal regions of AAF are poorly driven by tones (Figure 2D and Issa et al., 2014, Figure S2 and Figure S4). This discrepancy may originate from a number of key factors: recording depth, spatial resolution, and GCaMP sensitivity. This study focused on superficial layers as opposed to the thalamorecipient layer 4 that is often targeted in microelectrode mapping studies. A recent study examined the consequences of these laminar differences by performing multiunit recordings across layers of auditory cortex (Guo et al., 2012). They found that superficial neurons (as opposed to those in layer 4) are less likely to be tuned to pure tones. Indeed, the same study observed a fraction of recording sites in superficial layers that responded to tones but in an irregular manner. It is tempting to speculate that such recordings may resemble neuron 8 of Figure 5 from the present manuscript: a neuron with irregular tone responses but robust tuning to FM sweep rate. Further, a study in rat auditory cortex found that responses in superficial layers to tones and clicks were much sparser (Sakata and Harris, 2009), leaving the door open for other stimuli that could drive such neurons more robustly.

Another key factor in the delineation and localization of FM sweep rate organization may be the spatial resolution of the mapping method used. As illustrated in Figure 4H, FM sweep rate gradients are only on the order of ~250 μm in size. Coupled with the low sensitivity of GCaMP3 for individual spikes, it is conceivable that weakly responsive neurons or groups of neurons that are resolved with multiunit recordings may be largely missed under fluorescence imaging. Alternatively, it could be that the high mapping resolution offered by Ca^{2+} imaging is necessary to resolve fine organizational features. It is worth mentioning that mapping studies in rats do observe a tone insensitive region extending dorsocaudally from AAF (Kalatsky et al., 2005; Polley et al., 2007), but whether there is enough species homology to warrant a comparison to mice is unclear.

Instead, we found that tone insensitive regions responded to fast-FM sweeps. One of these regions, which we refer to as CSR, sits just dorsal to AII. In a previous study this region had been observed to respond to ultrasonic vocalizations (Issa et al., 2014), a perhaps unsurprising result given the prevalence of frequency modulations in mouse calls (Grimsley et al., 2011). Note however that the FM sweeps utilized in the present study covered a broad

range of frequencies (5 octaves) and rates (8 to 670 octaves/s). In contrast, adult mouse vocalizations utilize FM sweep rates in the range of 10 to 35 octaves/s (Grimsley et al., 2011) and bird chirps taken from field recordings are roughly in the range of 5 to 50 octaves/s (Bar-Yosef et al., 2002) (statistics were reported in linear Hz/s, so these numbers are estimates). Our study identified a more continuous and broad representation of FM sweep rates with some neurons tuned to sweep rates greater than 100 octaves/s. Other studies employing fast logarithmic sweeps in ferret AI (Nelken and Versnel, 2000) and rat inferior colliculus (Felsheim and Ostwald, 1996) have also found neurons tuned to such high sweep rates. Future work will be needed to relate the FM sweep rate mapping of the present study with the potentially behaviorally relevant processing of communication calls or other ethologically-relevant sounds.

As for the location of CSR, a nearby “dorsoanterior field” (DA) was found to be responsive to reversals in FM sweep direction (Tsukano et al., 2016, 2015). It remains to be determined if DA and CSR are related since FM sweeps used in those studies included direction reversals and superimposed sweeps and were at their fastest about 5 oct/s, slower than any of the FM stimuli used in this current study. In addition, a prior microelectrode study observed a preference for frequency modulations in UF (Stiebler et al., 1997), which may at least partially overlap with CSR. It is tempting to speculate about the relation of CSR to FM areas found in other species, such as the FM-FM area of bats (Suga et al., 1983), but first a deeper understanding of the neuronal computations producing FM selectivity (Sadagopan and Wang, 2009) and connectivity patterns between CSR and subcortical regions (Clopton and Winfield, 1974; Poon and Yu, 2000) are needed. Selectivity for FM sweep rate and direction could be inherited primarily from subcortical inputs (Covey and Casseday, 1999) or computed through intracortical circuits (Zhang et al., 2003). Another avenue to be explored is a comparison of left and right auditory cortices, as studies in rats (Rybalko et al., 2006), Mongolian gerbils (Wetzel et al., 1998), and humans (Poeppel et al., 2004) have all observed a lateralization of cortical FM sweep processing. The present study was conducted exclusively in the left hemisphere.

Our findings also indicate that neurons in cortex can be classified according to their sensitivity to broad classes of stimuli: these include (1) a frequency-selective group with strong tone responses and noise and sweep responses that may correspond to the frequency selectivity of the neuron; (2) a frequency-sweep selective group that respond specifically to the ordered presentation of a range of frequencies, as it occurs in a frequency sweep or a natural vocalization; and (3) a broadband responsive group that responds to broadband stimuli without the ordered nature of sweeps, but is weakly responsive to narrowband stimuli such as tones and frequency sweeps. These classes of neurons could represent parallel analysis channels in auditory cortex with sensitivity to distinct classes of sounds. Their identification may point the way to understanding the organization of auditory processing in cortex, in the way that different modules have been defined in visual cortex (Goodale and Milner, 1992; Wang and Burkhalter, 2007) or different modalities coupled to peripheral receptor sensitivity in somatosensory cortex (Mountcastle, 1957). The FM regions we have observed are one such higher-order modality involved in sound processing, but our results beg two questions: (1) are there other modules that can be identified with a broader class of stimuli; and (2) are these modules created in cortex or can similar stimulus selectivity be

identified in the auditory midbrain or below, as in the bat auditory system (Wenstrup and Portfors, 2011). Identification of these modules and whether they are processed in cortex will not only provide a deeper understanding of the function of auditory cortex in rodents but also enrich potential studies on cortical development and experience-dependent plasticity.

Acknowledgments

We wish to thank Manu Ben-Johny, Dwight Bergles, and Xiaoqin Wang for valuable discussions on the manuscript, members of the Calcium Signals Lab for their continued support, and Loren Looger and others from the GENIE Project for providing GCaMP6s transgenic mice. Most of all, however, we thank David Yue for giving us the opportunity to labor arm-in-arm beside him in pursuit of science and truth. Along the way, we got to know David not just as a scientific genius but also as a caring and humble man whose excitement for discovery was unmatched. He passed away on December 23, 2014, but our treasured memories of him and his impact as a scientist, professor, and friend will live on.

This work was supported by the Kleberg Foundation (D.T.Y.), NIH NINDS grant NS073874 (D.T.Y.), NIH NIMH grant MH065531 (D.T.Y.), MSTP fellowship (J.B.I.), and NRSA fellowship (B.D.H.).

REFERENCES

Altmann CF, Gaese BH. Representation of frequency-modulated sounds in the human brain. Hear. Res. 2014; 307:74–85. [PubMed: 23933098]

Arad N, Reisfeld D. Image Warping Using Few Anchor Points and Radial Functions. Comput. Graph. Forum. 1995; 14:35–46.

Bar-Yosef O, Rotman Y, Nelken I. Responses of neurons in cat primary auditory cortex to bird chirps: effects of temporal and spectral context. J. Neurosci. Off. J. Soc. Neurosci. 2002; 22:8619–8632.

Bendor D, Wang X. The Neuronal Representation of Pitch in Primate Auditory Cortex. Nature. 2005; 436:1161–1165. [PubMed: 16121182]

Bonin V, Histed MH, Yurgenson S, Reid RC. Local Diversity and Fine-Scale Organization of Receptive Fields in Mouse Visual Cortex. J. Neurosci. 2011; 31:18506–18521. [PubMed: 22171051]

Buonomano DV, Merzenich MM. Cortical plasticity: from synapses to maps. Annu. Rev. Neurosci. 1998; 21:149–186. [PubMed: 9530495]

Cavoretto R, De Rossi A, Quatember B. Landmark-Based Registration Using a Local Radial Basis Function Transformation. JNAIAM. 2011; 5:141–152.

Chechik G, Anderson MJ, Bar-Yosef O, Young ED, Tishby N, Nelken I. Reduction of information redundancy in the ascending auditory pathway. Neuron. 2006; 51:359–368. [PubMed: 16880130]

Chen T-W, Wardill TJ, Sun Y, Pulver SR, Renninger SL, Baohan A, Schreiter ER, Kerr RA, Orger MB, Jayaraman V, Looger LL, Svoboda K, Kim DS. Ultrasensitive fluorescent proteins for imaging neuronal activity. Nature. 2013; 499:295–300. [PubMed: 23868258]

Chi T, Ru P, Shamma SA. Multiresolution spectrotemporal analysis of complex sounds. J. Acoust. Soc. Am. 2005; 118:887–906. [PubMed: 16158645]

Clopton BM, Winfield JA. Unit responses in the inferior colliculus of rat to temporal auditory patterns of tone sweeps and noise bursts. Exp. Neurol. 1974; 42:532–540. [PubMed: 4828674]

Covey E, Casseday JH. Timing in the auditory system of the bat. Annu. Rev. Physiol. 1999; 61:457–476. [PubMed: 10099697]

Dana H, Chen T-W, Hu A, Shields BC, Guo C, Looger LL, Kim DS, Svoboda K. Thy1-GCaMP6 transgenic mice for neuronal population imaging in vivo. PloS One. 2014; 9:e108697. [PubMed: 25250714]

de Villers-Sidani E, Simpson KL, Lu Y-F, Lin RCS, Merzenich MM. Manipulating critical period closure across different sectors of the primary auditory cortex. Nat. Neurosci. 2008; 11:957–965. [PubMed: 18604205]

Felsheim C, Ostwald J. Responses to exponential frequency modulations in the rat inferior colliculus. Hear. Res. 1996; 98:137–151. [PubMed: 8880188]

Froudarakis E, Berens P, Ecker AS, Cotton RJ, Sinz FH, Yatsenko D, Saggau P, Bethge M, Tolias AS. Population code in mouse V1 facilitates readout of natural scenes through increased sparseness. Nat. Neurosci. 2014; 17:851–857. [PubMed: 24747577]

Goodale MA, Milner AD. Separate visual pathways for perception and action. Trends Neurosci. 1992; 15:20–25. [PubMed: 1374953]

Gorski JA, Talley T, Qiu M, Puelles L, Rubenstein JLR, Jones KR. Cortical excitatory neurons and glia, but not GABAergic neurons, are produced in the Emx1-expressing lineage. J. Neurosci. Off. J. Soc. Neurosci. 2002; 22:6309–6314.

Grimsley JMS, Monaghan JJM, Wenstrup JJ. Development of social vocalizations in mice. PloS One. 2011; 6:e17460. [PubMed: 21408007]

Guo W, Chambers AR, Darrow KN, Hancock KE, Shinn-Cunningham BG, Polley DB. Robustness of cortical topography across fields, laminae, anesthetic states, and neurophysiological signal types. J. Neurosci. Off. J. Soc. Neurosci. 2012; 32:9159–9172.

Hackett TA, Rinaldi Barkat T, O'Brien BMJ, Hensch TK, Polley DB. Linking Topography to Tonotopy in the Mouse Auditory Thalamocortical Circuit. J. Neurosci. 2011; 31:2983–2995. [PubMed: 21414920]

Haeffele, B.; Young, E.; Vidal, R. Structured Low-Rank Matrix Factorization: Optimality, Algorithm, and Applications to Image Processing. Proceedings of the 31st International Conference on Machine Learning (ICML-14); Presented at the Proceedings of the 31st International Conference on Machine Learning (ICML-14); 2014. p. 2007-2015.

Hofer SB, Ko H, Pichler B, Vogelstein J, Ros H, Zeng H, Lein E, Lesica NA, Mrsic-Flogel TD. Differential connectivity and response dynamics of excitatory and inhibitory neurons in visual cortex. Nat. Neurosci. 2011; 14:1045–1052. [PubMed: 21765421]

Holy TE, Guo Z. Ultrasonic Songs of Male Mice. PLoS Biol. 2005; 3

Honma Y, Tsukano H, Horie M, Ohshima S, Tohmi M, Kubota Y, Takahashi K, Hishida R, Takahashi S, Shibuki K. Auditory Cortical Areas Activated by Slow Frequency-Modulated Sounds in Mice. PLoS ONE. 2013; 8:e68113. [PubMed: 23874516]

Issa JB, Haeffele BD, Agarwal A, Bergles DE, Young ED, Yue DT. Multiscale optical ca(2+) imaging of tonal organization in mouse auditory cortex. Neuron. 2014; 83:944–959. [PubMed: 25088366]

Kaas, JH. The Evolution of Auditory Cortex: The Core Areas. In: Winer, JA.; Schreiner, CE., editors. The Auditory Cortex. US: Springer; 2011. p. 407-427.

Kalatsky VA, Polley DB, Merzenich MM, Schreiner CE, Stryker MP. Fine functional organization of auditory cortex revealed by Fourier optical imaging. Proc. Natl. Acad. Sci. U. S. A. 2005; 102:13325–13330. [PubMed: 16141342]

Karmarkar UR, Dan Y. Experience-dependent plasticity in adult visual cortex. Neuron. 2006; 52:577–585. [PubMed: 17114043]

King AJ, Nelken I. Unraveling the principles of auditory cortical processing: can we learn from the visual system? Nat. Neurosci. 2009; 12:698–701. [PubMed: 19471268]

Klug A, Grothe B. Ethological stimuli. Oxf. Handb. Audit. Sci. Audit. Brain. 2010; 2:173.

Ko H, Hofer SB, Pichler B, Buchanan KA, Sjöström PJ, Mrsic-Flogel TD. Functional specificity of local synaptic connections in neocortical networks. Nature. 2011; 473:87–91. [PubMed: 21478872]

Letzkus JJ, Wolff SBE, Meyer EMM, Tovote P, Courtin J, Herry C, Lüthi A. A disinhibitory microcircuit for associative fear learning in the auditory cortex. Nature. 2011; 480:331–335. [PubMed: 22158104]

Linden JF, Liu RC, Sahani M, Schreiner CE, Merzenich MM. Spectrotemporal structure of receptive fields in areas AI and AAF of mouse auditory cortex. J. Neurophysiol. 2003; 90:2660–2675. [PubMed: 12815016]

Lucy LB. An iterative technique for the rectification of observed distributions. Astron. J. 1974; 79:745.

May B, Moody DB, Stebbins WC. Categorical perception of conspecific communication sounds by Japanese macaques, Macaca fuscata. J. Acoust. Soc. Am. 1989; 85:837–847. [PubMed: 2925998]

Mendelson JR, Schreiner CE, Sutter ML, Grasse KL. Functional topography of cat primary auditory cortex: responses to frequency-modulated sweeps. Exp. Brain Res. 1993; 94:65–87. [PubMed: 8335076]

Moore, BCJ. Hearing. Academic Press; 1995.

Mountcastle VB. Modality and topographic properties of single neurons of cat's somatic sensory cortex. J. Neurophysiol. 1957; 20:408–434. [PubMed: 13439410]

Nelken I, Versnel H. Responses to linear and logarithmic frequency-modulated sweeps in ferret primary auditory cortex. Eur. J. Neurosci. 2000; 12:549–562. [PubMed: 10712634]

Neunuebel JP, Taylor AL, Arthur BJ, Egnor SER. Female mice ultrasonically interact with males during courtship displays. eLife. 2015; 4

Neuweiler G. Foraging ecology and audition in echolocating bats. Trends Ecol. Evol. 1989; 4:160–166. [PubMed: 21227342]

Norman-Haignere S, Kanwisher NG, McDermott JH. Distinct Cortical Pathways for Music and Speech Revealed by Hypothesis-Free Voxel Decomposition. Neuron. 2015; 88:1281–1296. [PubMed: 26687225]

Ohl FW, Wetzel W, Wagner T, Rech A, Scheich H. Bilateral ablation of auditory cortex in Mongolian gerbil affects discrimination of frequency modulated tones but not of pure tones. Learn. Mem. Cold Spring Harb. N. 1999; 6:347–362.

Orduña I, Mercado E, Gluck MA, Merzenich MM. Spectrotemporal sensitivities in rat auditory cortical neurons. Hear. Res. 2001; 160:47–57. [PubMed: 11591490]

Petreanu L, Gutnisky DA, Huber D, Xu N, O'Connor DH, Tian L, Looger L, Svoboda K. Activity in motor-sensory projections reveals distributed coding in somatosensation. Nature. 2012; 489:299–303. [PubMed: 22922646]

Pistorio AL, Vintch B, Wang X. Acoustic analysis of vocal development in a New World primate, the common marmoset (Callithrix jacchus). J. Acoust. Soc. Am. 2006; 120:1655–1670. [PubMed: 17004487]

Poeppel D, Guillemin A, Thompson J, Fritz J, Bavelier D, Braun AR. Auditory lexical decision, categorical perception, and FM direction discrimination differentially engage left and right auditory cortex. Neuropsychologia. 2004; 42:183–200. [PubMed: 14644105]

Polley DB, Read HL, Storace DA, Merzenich MM. Multiparametric auditory receptive field organization across five cortical fields in the albino rat. J. Neurophysiol. 2007; 97:3621–3638. [PubMed: 17376842]

Poon PW, Yu PP. Spectro-temporal receptive fields of midbrain auditory neurons in the rat obtained with frequency modulated stimulation. Neurosci. Lett. 2000; 289:9–12. [PubMed: 10899396]

Portfors CV. Types and functions of ultrasonic vocalizations in laboratory rats and mice. J. Am. Assoc. Lab. Anim. Sci. JAALAS. 2007; 46:28–34. [PubMed: 17203913]

Rajasethupathy P, Sankaran S, Marshel JH, Kim CK, Ferenczi E, Lee SY, Berndt A, Ramakrishnan C, Jaffe A, Lo M, Liston C, Deisseroth K. Projections from neocortex mediate top-down control of memory retrieval. Nature. 2015; 526:653–659. [PubMed: 26436451]

Rauschecker JP. Cortical processing of complex sounds. Curr. Opin. Neurobiol. 1998; 8:516–521. [PubMed: 9751652]

Rauschecker JP, Scott SK. Maps and streams in the auditory cortex: nonhuman primates illuminate human speech processing. Nat. Neurosci. 2009; 12:718–724. [PubMed: 19471271]

Richardson WH. Bayesian-Based Iterative Method of Image Restoration. J. Opt. Soc. Am. 1972; 62:55–59.

Rybalko N, Suta D, Nwabueze-Ogbo F, Syka J. Effect of auditory cortex lesions on the discrimination of frequency-modulated tones in rats. Eur. J. Neurosci. 2006; 23:1614–1622. [PubMed: 16553625]

Sadagopan S, Wang X. Nonlinear spectrotemporal interactions underlying selectivity for complex sounds in auditory cortex. J. Neurosci. Off. J. Soc. Neurosci. 2009; 29:11192–11202.

Sakata S, Harris KD. Laminar Structure of Spontaneous and Sensory-Evoked Population Activity in Auditory Cortex. Neuron. 2009; 64:404–418. [PubMed: 19914188]

Schneider DM, Nelson A, Mooney R. A synaptic and circuit basis for corollary discharge in the auditory cortex. Nature. 2014; 513:189–194. [PubMed: 25162524]

Singh NC, Theunissen FE. Modulation spectra of natural sounds and ethological theories of auditory processing. J. Acoust. Soc. Am. 2003; 114:3394–3411. [PubMed: 14714819]

Smetters D, Majewska A, Yuste R. Detecting action potentials in neuronal populations with calcium imaging. Methods San Diego Calif. 1999; 18:215–221.

Stiebler I, Neulist R, Fichtel I, Ehret G. The auditory cortex of the house mouse: left-right differences, tonotopic organization and quantitative analysis of frequency representation. J. Comp. Physiol. [A]. 1997; 181:559–571.

Suga N, O'Neill WE, Kujirai K, Manabe T. Specificity of combination-sensitive neurons for processing of complex biosonar signals in auditory cortex of the mustached bat. J. Neurophysiol. 1983; 49:1573–1626. [PubMed: 6875639]

Taberner AM, Liberman MC. Response properties of single auditory nerve fibers in the mouse. J. Neurophysiol. 2005; 93:557–569. [PubMed: 15456804]

Tian B, Rauschecker JP. Processing of frequency-modulated sounds in the lateral auditory belt cortex of the rhesus monkey. J. Neurophysiol. 2004; 92:2993–3013. [PubMed: 15486426]

Tian L, Hires SA, Mao T, Huber D, Chiappe ME, Chalasani SH, Petreanu L, Akerboom J, McKinney SA, Schreiter ER, Bargmann CI, Jayaraman V, Svoboda K, Looger LL. Imaging neural activity in worms, flies and mice with improved GCaMP calcium indicators. Nat. Methods. 2009; 6:875–881. [PubMed: 19898485]

Trujillo M, Measor K, Carrasco MM, Razak KA. Selectivity for the rate of frequency-modulated sweeps in the mouse auditory cortex. J. Neurophysiol. 2011; 106:2825–2837. [PubMed: 21849608]

Tsukano H, Horie M, Bo T, Uchimura A, Hishida R, Kudoh M, Takahashi K, Takebayashi H, Shibuki K. Delineation of a frequency-organized region isolated from the mouse primary auditory cortex. J. Neurophysiol. 2015; 113:2900–2920. [PubMed: 25695649]

Tsukano H, Horie M, Hishida R, Takahashi K, Takebayashi H, Shibuki K. Quantitative map of multiple auditory cortical regions with a stereotaxic fine-scale atlas of the mouse brain. Sci. Rep. 2016; 6:22315. [PubMed: 26924462]

Vogelstein JT, Packer AM, Machado TA, Sippy T, Babadi B, Yuste R, Paninski L. Fast nonnegative deconvolution for spike train inference from population calcium imaging. J. Neurophysiol. 2010; 104:3691–3704. [PubMed: 20554834]

Von Békésy, G. Experiments in hearing. Oxford, England: Mcgraw Hill; 1960.

Wang Q, Burkhalter A. Area map of mouse visual cortex. J. Comp. Neurol. 2007; 502:339–357. [PubMed: 17366604]

Wekselblatt JB, Flister ED, Piscopo DM, Niell CM. Large-scale imaging of cortical dynamics during sensory perception and behavior. J. Neurophysiol. 2016

Wenstrup JJ, Portfors CV. Neural processing of target distance by echolocating bats: functional roles of the auditory midbrain. Neurosci. Biobehav. Rev. 2011; 35:2073–2083. [PubMed: 21238485]

Wetzel W, Ohl FW, Wagner T, Scheich H. Right auditory cortex lesion in Mongolian gerbils impairs discrimination of rising and falling frequency-modulated tones. Neurosci. Lett. 1998; 252:115–118. [PubMed: 9756335]

Zariwala HA, Borghuis BG, Hoogland TM, Madisen L, Tian L, De Zeeuw CI, Zeng H, Looger LL, Svoboda K, Chen T-W. A Cre-dependent GCaMP3 reporter mouse for neuronal imaging in vivo. J. Neurosci. Off. J. Soc. Neurosci. 2012; 32:3131–3141.

Zhang LI, Tan AYY, Schreiner CE, Merzenich MM. Topography and synaptic shaping of direction selectivity in primary auditory cortex. Nature. 2003; 424:201–205. [PubMed: 12853959]

Zhu Y, Romero MI, Ghosh P, Ye Z, Charnay P, Rushing EJ, Marth JD, Parada LF. Ablation of NF1 function in neurons induces abnormal development of cerebral cortex and reactive gliosis in the brain. Genes Dev. 2001; 15:859–876. [PubMed: 11297510]

Highlights

- Responses to sounds were measured using multiscale Ca^{2+} imaging of auditory cortex.
- Regions responding to tones responded to slow frequency modulated (FM) sweeps.
- Regions unresponsive to tones instead responded to fast FM sweeps.
- Fast-FM neurons were not responsive to bandlimited noise.

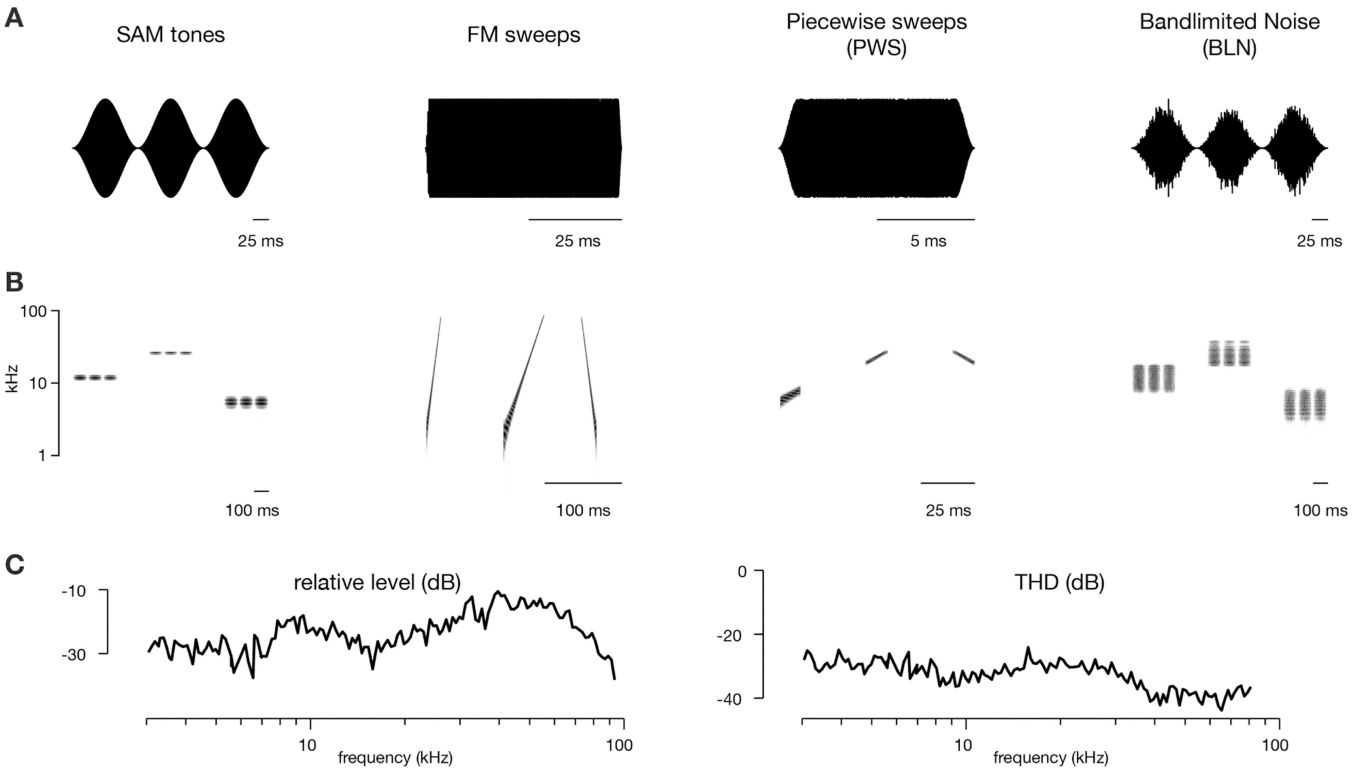

Figure 1. Stimulus waveforms and spectrograms

(A) Waveforms of acoustic stimuli used in this study.

(B) Spectrograms of corresponding stimulus classes. Shown are three stimuli for each class, which were presented in random order (in actual trials, 16 to 30 stimuli were used). For SAM tones, piecewise sweeps, and bandlimited noise, the center frequency of the stimulus was changed. For FM sweeps, the sweep rate was changed.

(C) Relative frequency response curve (left) and total harmonic distortion (THD, right, acquired at 20 dB attenuation level) for speaker used in this study.

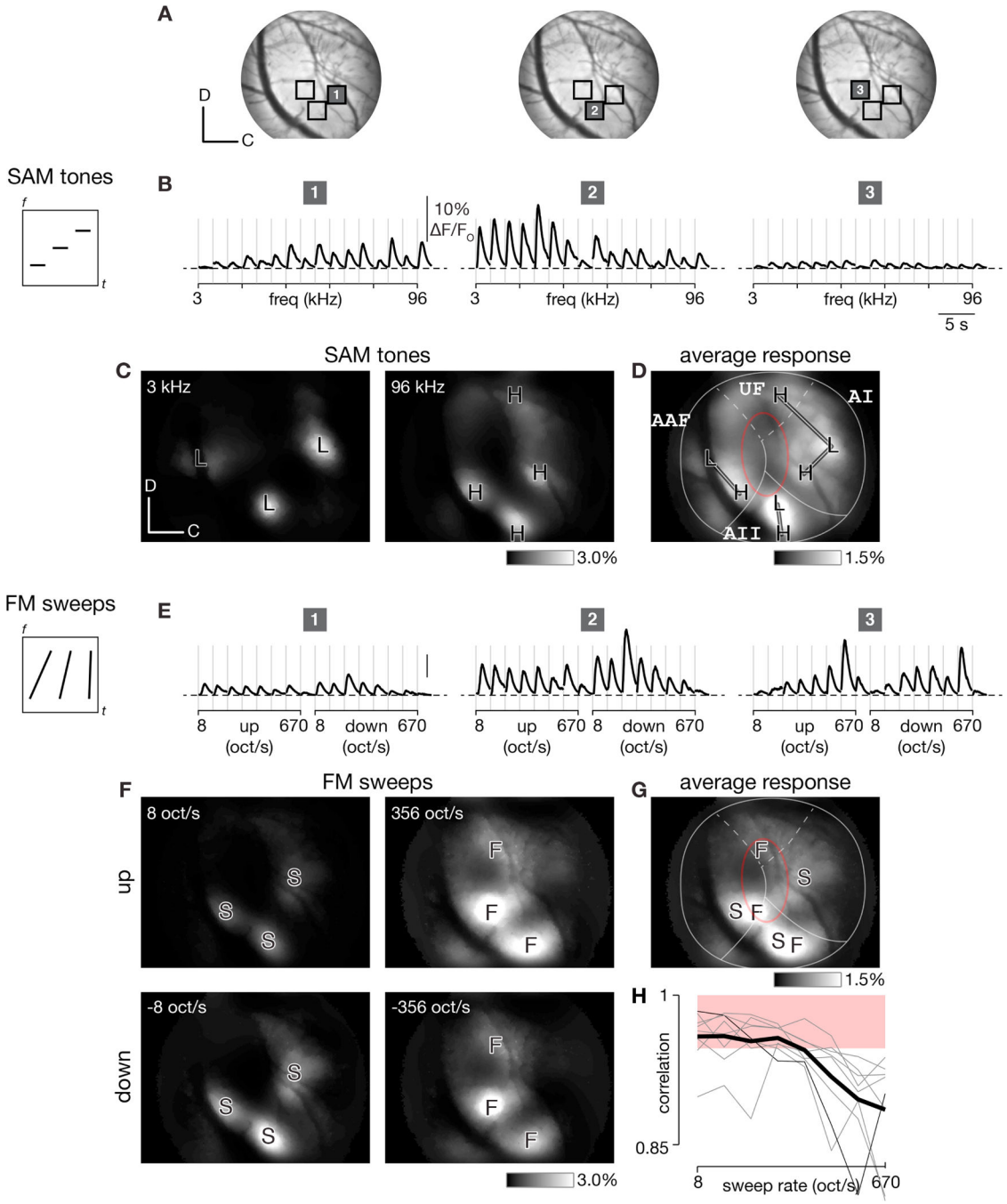

Figure 2. Transcranial responses to SAM tones and FM sweeps in GCaMP3 mice

(A) Average transcranial fluorescence image of auditory cortex in exemplar mouse expressing GCaMP3 under Syn1-Cre driver line. Dorsal-caudal orientation and 400 μm scale on lower left.

(B) Ca^{2+} activity induced by SAM tones at −20 dB attenuation (top) at the three regions marked in panel A. Stimuli were played in random order (represented by spectrogram on left for three stimuli) and responses sorted by increasing frequency (3 to 96 kHz). Traces show

baseline-corrected deblurred signals for each ~100 × 100 μm^2 region after denoising with a sparse encoding algorithm (Haeffele et al., 2014).

(C) Spatial maps depicting responses to low (3 kHz, left) and high (96 kHz, right) frequency SAM tones. 'L' and 'H' landmarks mark centers of regions with strongest responses to low and high frequency tones, respectively. Images show average response to each stimulus after processing by sparse-encoding algorithm and deblurring. Dorsal-caudal orientation and 300 μm scale denoted on lower left.

(D) Average response across all SAM tones (16 300-ms tones logarithmically spaced from 3–96 kHz with 10 Hz modulation). Lines indicate tonotopic axes and red oval highlights tone-insensitive area.

(E) Ca^{2+} activity induced by FM sweeps at −40 dB attenuation at the three regions marked in panel A. Responses to randomly ordered stimuli (represented by spectrogram on left for three different sweep rates) sorted by rate (8 to 670 oct/s) and direction of FM sweep.

(F) Responses to slow (left) and fast (right) FM sweeps in the upward (top row) or downward (bottom row) direction. 'S' and 'F' landmarks mark centers of regions responding best to slow and fast sweeps, respectively.

(G) Average response across all FM sweeps (stimuli logarithmically swept the same 5-octave range of 3 to 96 kHz but varied in rate from 8 to 670 oct/s and duration from 600 to 7.5 msec). (H) Spearman correlation between SAM tone and FM sweep responses as a function of sweep rate for 8 experiments (experiment corresponding to panels A-G in thin black, other individual experiments in gray, average in thick black). Shaded red region shows bootstrap-estimated 95% confidence interval derived from Spearman correlations between randomly sampled tone responses.

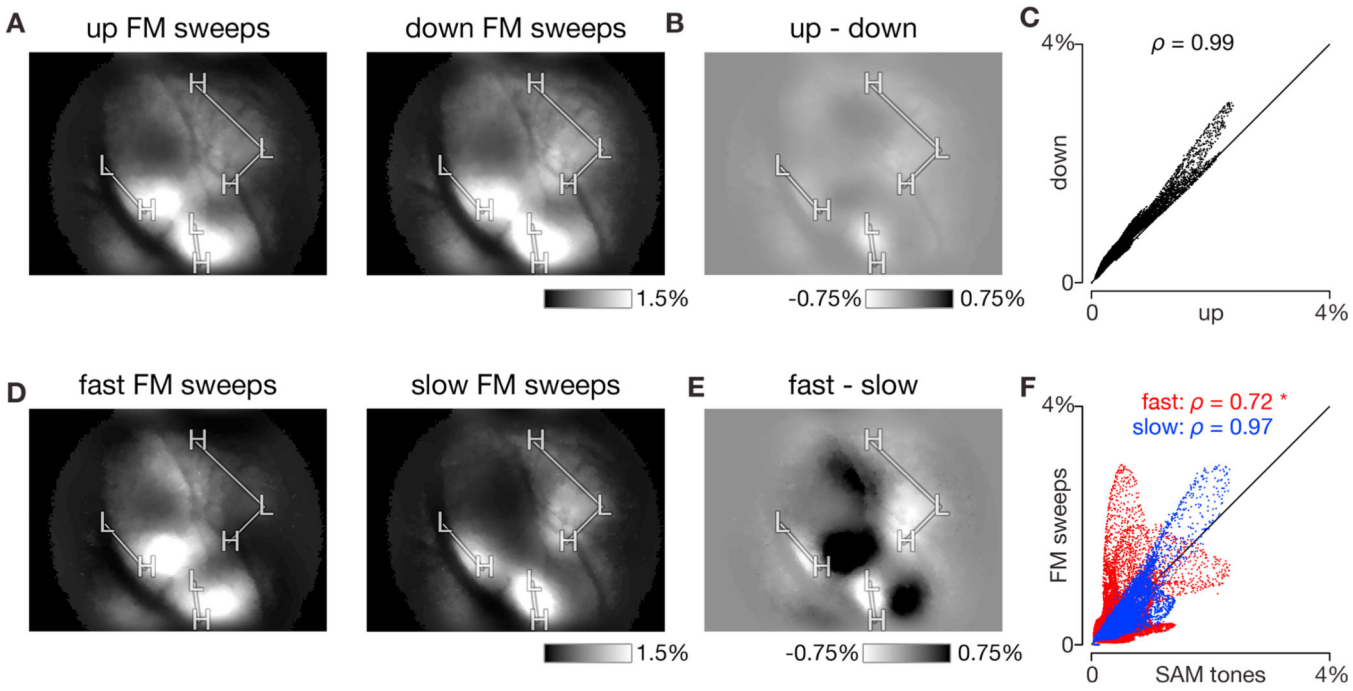

Figure 3. Dependence of FM sweep responses on direction and rate

(A) Average response to upward FM sweeps (left) and downward FM sweeps (right). Each condition averaged over all 8 sweep rates used. Same experiment as shown in Figure 2. Equivalent $\Delta F/F_O$ scale bar on lower right.

(B) Difference in response to up and down sweeps. Map generated by subtracting response to downward FM sweeps (right panel of A) from response to upward FM sweeps (left panel of A). Equivalent $\Delta F/F_O$ scale bar on lower right.

(C) Scatter plot of downward FM sweep response strength versus upward FM sweep response strength for each pixel. Response strengths taken directly from panel A. Spearman correlation displayed at top of plot.

(D) Average response to fast FM sweeps (left, 360 and 670 oct/s) and slow FM sweeps (right, 8 and 16 oct/s). Data averaged across up and down sweeps at −40 dB attenuation. Equivalent $\Delta F/F_O$ scale bar on lower right.

(E) Difference in response to fast and slow sweeps. Map generated by subtracting response to slow FM sweeps (left panel of D) from response to fast FM sweeps (right panel of D). Equivalent $\Delta F/F_O$ scale bar on lower right.

(F) Scatter plot of fast (red) and slow (blue) FM sweep response strengths versus SAM tone response strength for each pixel. Response strengths taken directly from panel D. Spearman correlation for each comparison displayed at top of each plot. Asterisk indicates that only red scatterplot (fast FM sweep versus SAM tone response) was significantly different (outside a 95% confidence interval) from the null distribution, which was estimated by Spearman correlations between randomly sampled SAM tone responses.

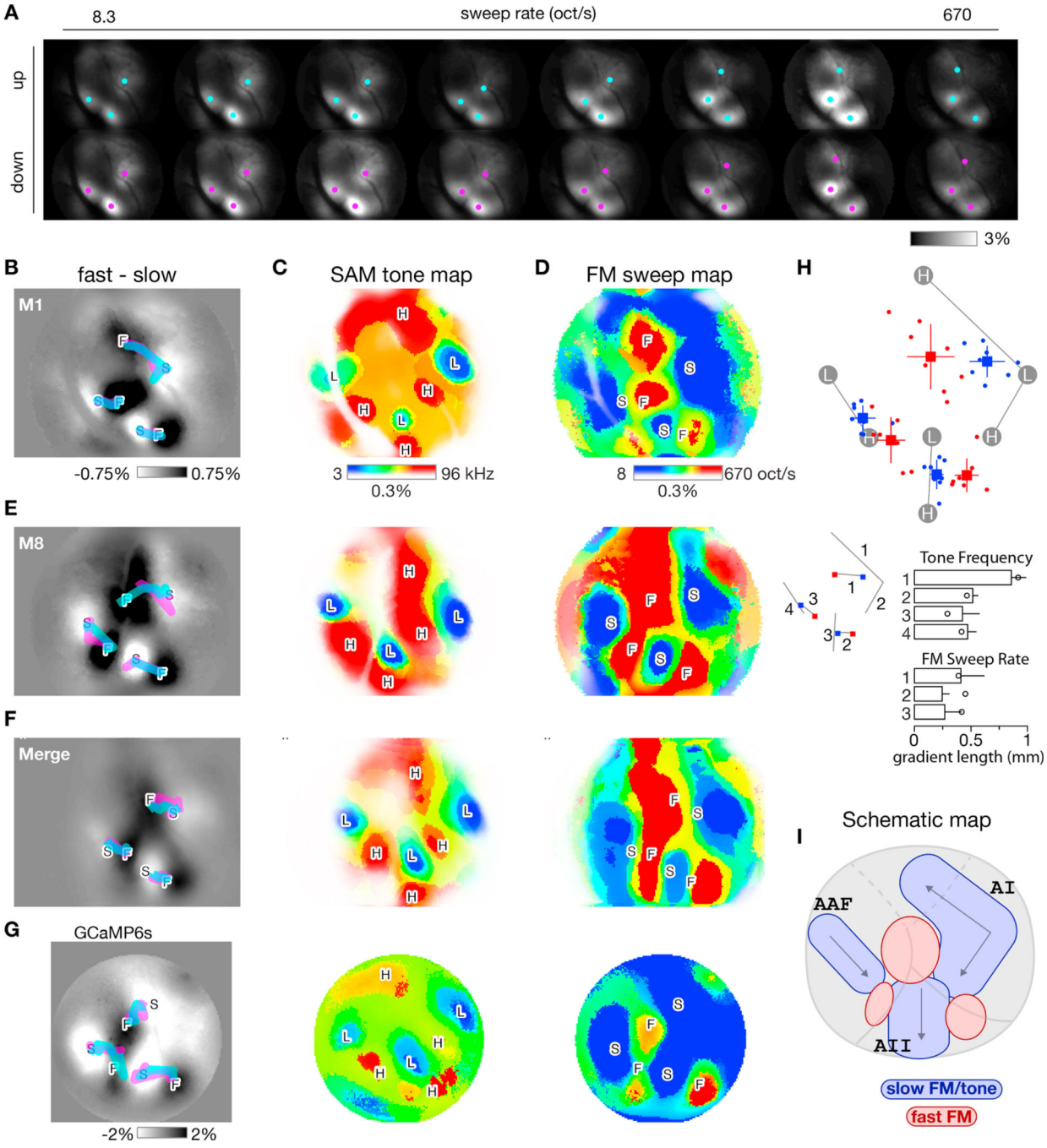

Figure 4. Formation of FM sweep maps and comparison across experiments

(A) Transcranial fluorescence responses during presentation of FM sweeps of various sweep rates (columns) and directions (rows). Images displayed as in Figure 2F. Equivalent $\Delta F/F_O$ scale bar on lower right. Same mouse as Figures 2 and 3 but now responses averaged over multiple sound levels. Cyan and magenta dots represent local center-of-mass of response peaks for up and down sweep responses, respectively.

(B) Difference in response between fast and slow FM sweeps, averaged over upward and downward sweeps for the 2 fastest (360 and 670 oct/s) and 2 slowest (8 and 16 oct/s) sweeps

tested. Thick cyan and magenta lines, derived from center-of-masses marked in A, track peak of responses to up and down sweeps as sweep rate increases from slow (S) to fast (F) sweeps.

(C) Best-frequency map derived from responses to individual SAM tones. Best frequency at each pixel approximated as weighted average of 3 frequencies eliciting largest responses at threshold sound level. Color map (right) indicates best-frequency color assignments (blue = low, red = high) and response strength (color saturation corresponds to response amplitude).

(D) Best-rate map derived from responses to individual FM sweeps. Format analogous to C except now pixel color indicates preferred rate of FM sweep (blue = slow, red = fast).

(E) Maps for one other experiment. Same format as panels B-D.

(F) Average of 8 individual transcranial response maps, including those in panels B-E, demonstrating preservation of overall canonical layout across mice. Landmark-based registration was used to morph each individual map onto a common coordinate system before averaging. Registration for both SAM tone maps and FM sweep maps was based on tone-map landmarks, which are derived from responses to low (L) and high (H) frequency SAM tones. Gradients were computed from the merged response maps. See panel H for gradients computed from the individual trajectories.

(G) Maps for a transgenic GCaMP6s mouse with a chronic window. SAM tone frequency maps averaged over 16 trials. FM sweep rate maps averaged over 14 trials.

(H) Layout of response peaks for slow (8 oct/s, blue) and fast (670 oct/s, red) FM sweeps across 8 experiments. Experiments where registered onto a common coordinate system based on tone-map landmarks. Dots indicate individual experiments; squares and lines indicate means and standard deviations. Lengths of each of the seven gradients (four for SAM tone frequency and three for FM sweep rate) are shown in the bar plots along with standard deviations. Circles denote gradient lengths for GCaMP6s experiment shown in panel G.

(I) Schematic of slow-FM sweep / SAM tone (blue shapes) and fast-FM sweep (red shapes) regions as they intersect with traditional boundaries of AI, AAF, and AII.

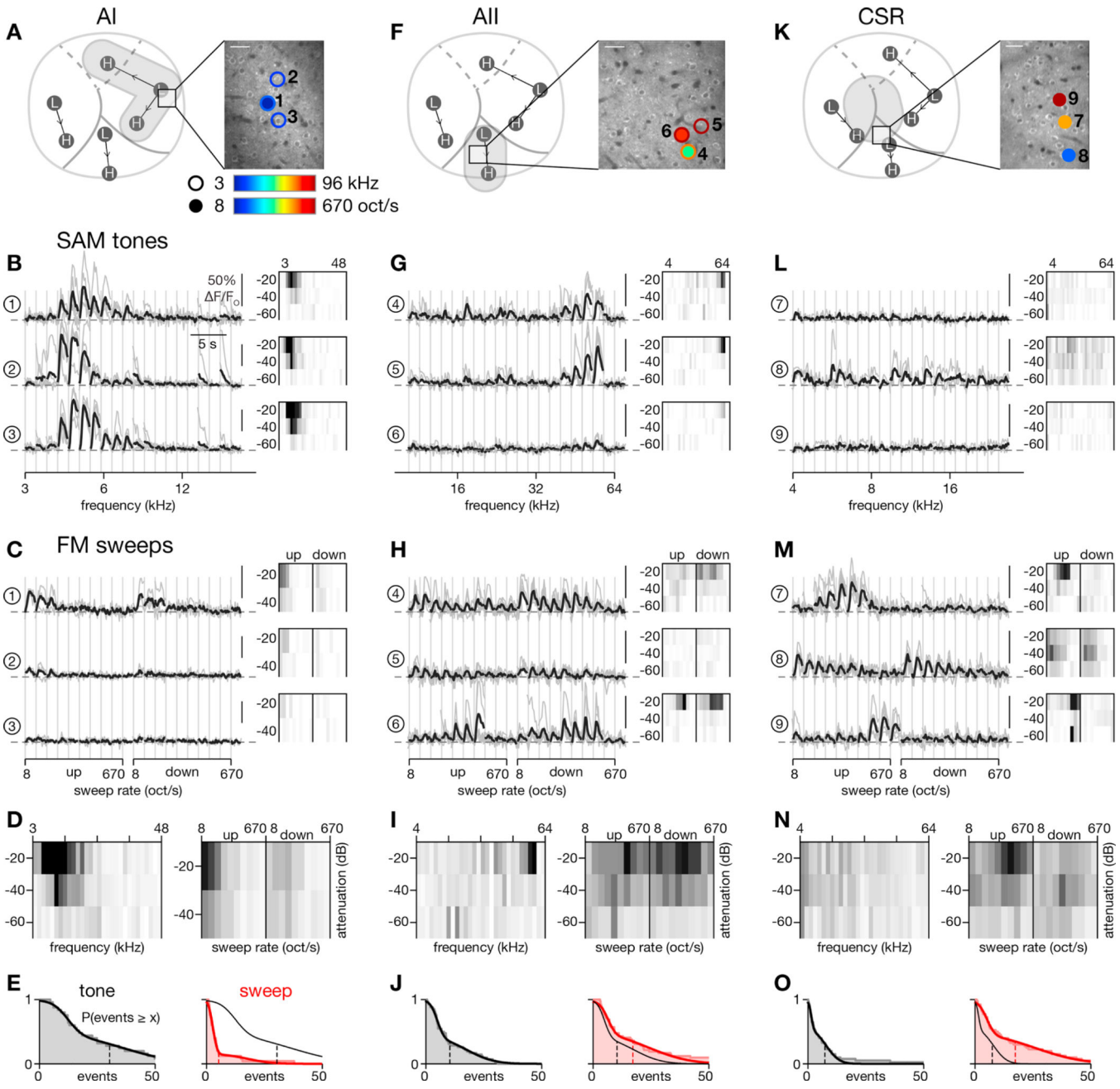

Figure 5. Differing tone-sweep response profiles for individual neurons across auditory cortex

(A–E) Characterization of tone and sweep tuning for two-photon imaging field in AI.

(A) Location of two-photon imaging field with respect to widefield imaging landmarks (left) and of individual neurons with respect to two-photon imaging field (right). Putative AI is indicated by gray shading (left). Two-photon imaging field is located near low-frequency pole of AI. Neurons to be scrutinized in panels B and C are indicated by circles. Circle outline color indicates best frequency of that neuron while fill color indicates preferred sweep rate. Lack of either outline or fill indicates that the neuron did not respond appreciably to tones or sweeps, respectively. Scale bar: 30 μm.

(B) SAM tone responses of the 3 neurons marked in panel A. Activity of neurons in response to −20 dB attenuated tones shown on left with individual trials in gray and response averaged across trials in black. Frequency response areas (FRAs), shown in thumbnails on the right, summarize responses across all frequencies (*x* axis) and sound levels (*y* axis) tested. Detailed axis labels given in panel D. FRAs scaled to 15 events/s.
(C) Responses for the 3 neurons in panel B to −20 dB attenuated FM sweeps. Sweep rate response areas (SRAs) scaled to 15 events/s.
(D) FRA (left) and SRA (right) averaged across all active neurons ($n = 25$ out of 47 total) in the field. Both images scaled to 3 events/s. Axis labels apply to FRA and SRA thumbnails above.
(E) Distributions of SAM tone (left, black; smoothed fit reproduced on right) and FM sweep (right, red) response strengths for all active neurons in the field. Response strength calculated as maximum total response above baseline (events/s summed across all frequencies or sweep rates tested for any attenuation level). Mean response indicated by vertical dashed line ($\mu_{tone} = 30.4$, $\mu_{sweep} = 5.3$). Tone responses were significantly stronger ($p < 1e\text{-}4$, 2-sided Wilcoxon signed-rank test).
(F–J) Tone and sweep responses for field in AII. Format identical to A-E except now gray shading in panel F, left, highlights tone-sensitive region of AII. Across all active neurons in this field ($n = 42$), responses to sweeps were stronger ($\mu_{tone} = 10.4$, $\mu_{sweep} = 17.3$; $p < 0.01$, 2-sided Wilcoxon signed-rank test).
(K–O) Responses for field in CSR. Left subpanel of K highlights in gray shading the location of a potential sweep region from widefield imaging results. Across all active neurons in this field ($n = 40$), responses to sweeps were significantly stronger ($\mu_{tone} = 7.4$, $\mu_{sweep} = 17.5$; $p < 1e\text{-}5$, 2-sided Wilcoxon signed-rank test).

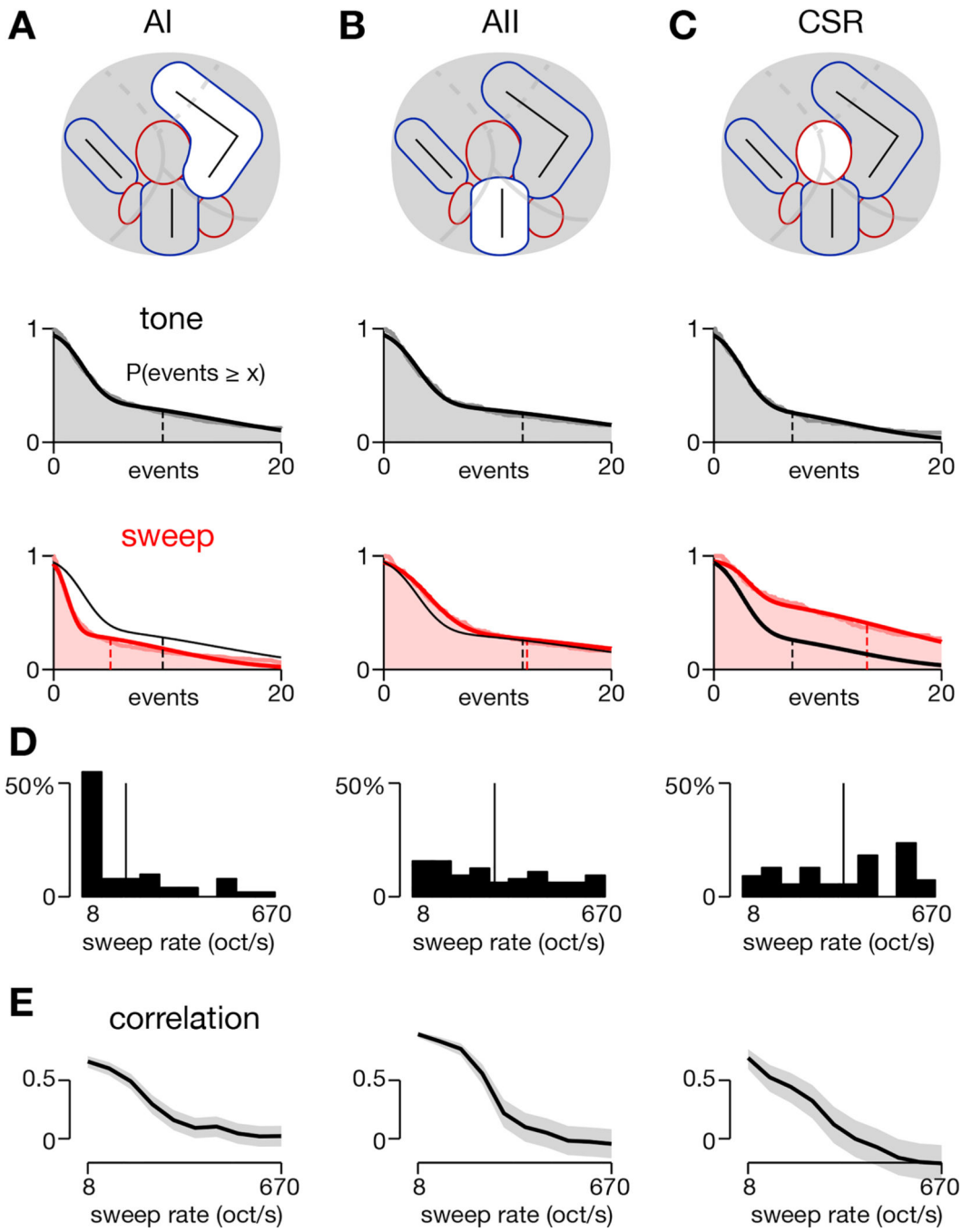

Figure 6. Differences in responses to tones and sweeps across three cortical regions

Average responses to tones and sweeps of individual neurons registered to AI, AII, and CSR. (A–C) Histograms demonstrating strength of responses to SAM tones and FM sweeps for neurons within each region. Schematized locations of these regions are shown in the top row. Histograms of tone responses are represented by gray shading with mean response indicated by dashed vertical line (middle row). Histograms of sweep responses are shown in red shading with mean response as dashed vertical red line and mean tone response shown again as dashed vertical black line (bottom row). AI: μ_{tone} = 9.6 (6.6), μ_{sweep} = 5.0 (2.9), p < 1e-26

($p < 1e-21$); AII: $\mu_{tone} = 12.2$ (10.0), $\mu_{sweep} = 12.6$ (10.0), $p = 0.047$ ($p = 0.6$); CSR, $\mu_{tone} = 6.9$ (4.2), $\mu_{sweep} = 13.5$ (7.0), $p < 1e-7$ ($p < 1e-4$). Numbers in parentheses are for neuropil-subtracted data. Statistical tests via 2-sided Wilcoxon signed-rank test.

(D) Distribution of preferred sweep rate for neurons in each region. For FM sweep-responsive neurons, the preferred sweep rate was computed for each neuron and binned into one of the 10 sweep rates tested. Thin vertical line indicates the mean sweep rate for each population (19.67 for AI, 52.12 for AII, and 83.76 oct/s for CSR).

(E) Correlation between FM sweep response and SAM tone response as a function of FM sweep rate. Maximum response at each stimulus condition used for calculations. Gray shading indicates 95% confidence intervals.

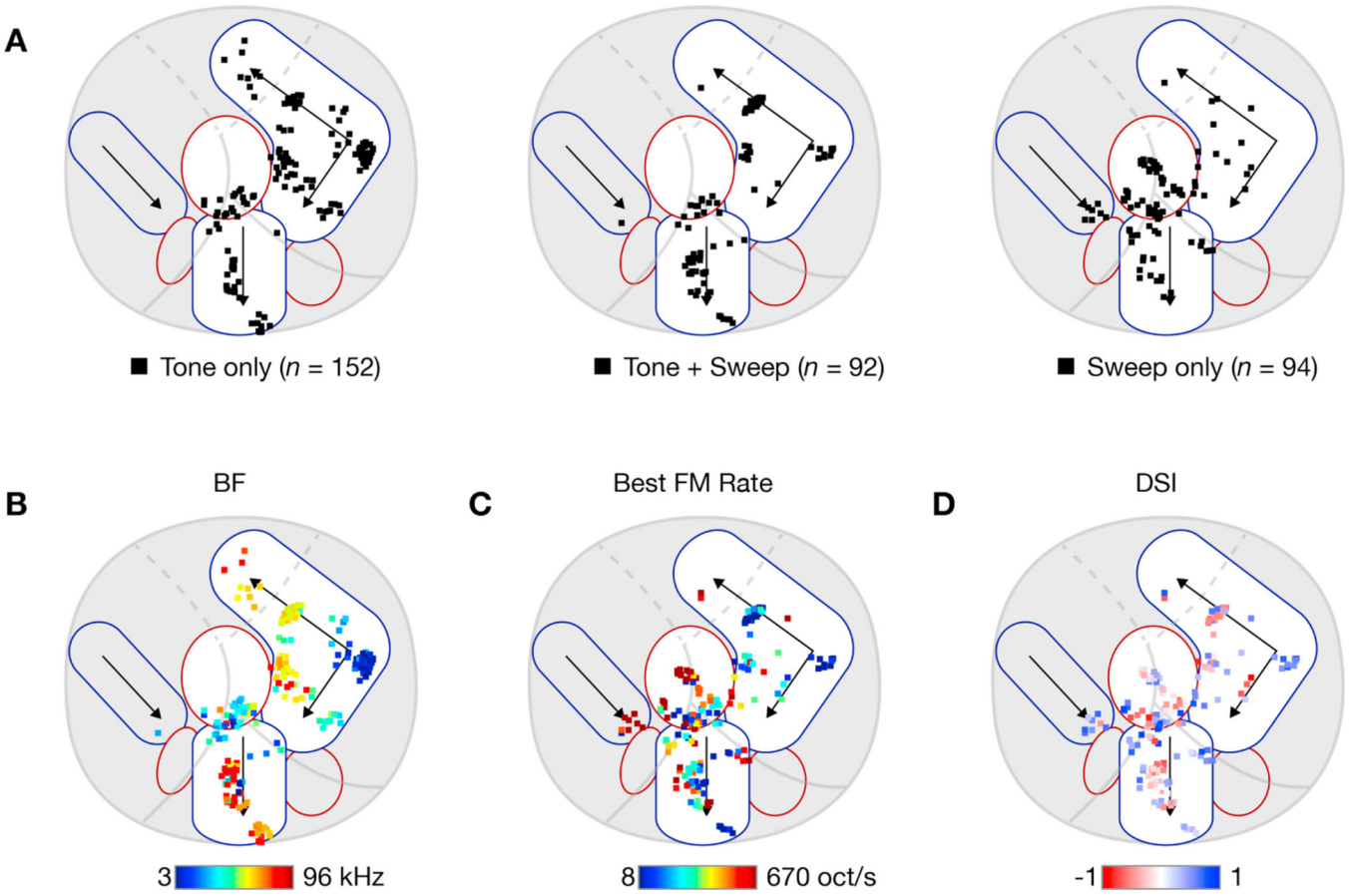

Figure 7. Distribution of tone and sweep neurons throughout auditory cortex

Individual neurons across all experiments were registered onto a common coordinate system to visualize the population data.

(A) Categorization of responsive neurons into 'Tone only' (left), 'Tone + Sweep' (middle), and 'Sweep only' (right) based on presence of significant responses to each class of stimuli (see Methods for criteria used). Plots are overlaid on schematic representation of mouse auditory cortex with separate tone (blue-outlined shapes) and sweep (red-outlined shapes) regions.

(B) Best frequency map at the level of individual neurons. For all tone-responsive neurons, the best frequency is color-coded according to the colorbar below.

(C) Best sweep-rate map. For all sweep-responsive neurons, the preferred FM sweep rate is color-coded according to the colorbar below.

(D) Direction selectivity map. For all sweep-responsive neurons, the DSI is color-coded according to the colorbar below. Saturation indicates DSI magnitude, with full saturation corresponding to a DSI of +1 or −1.

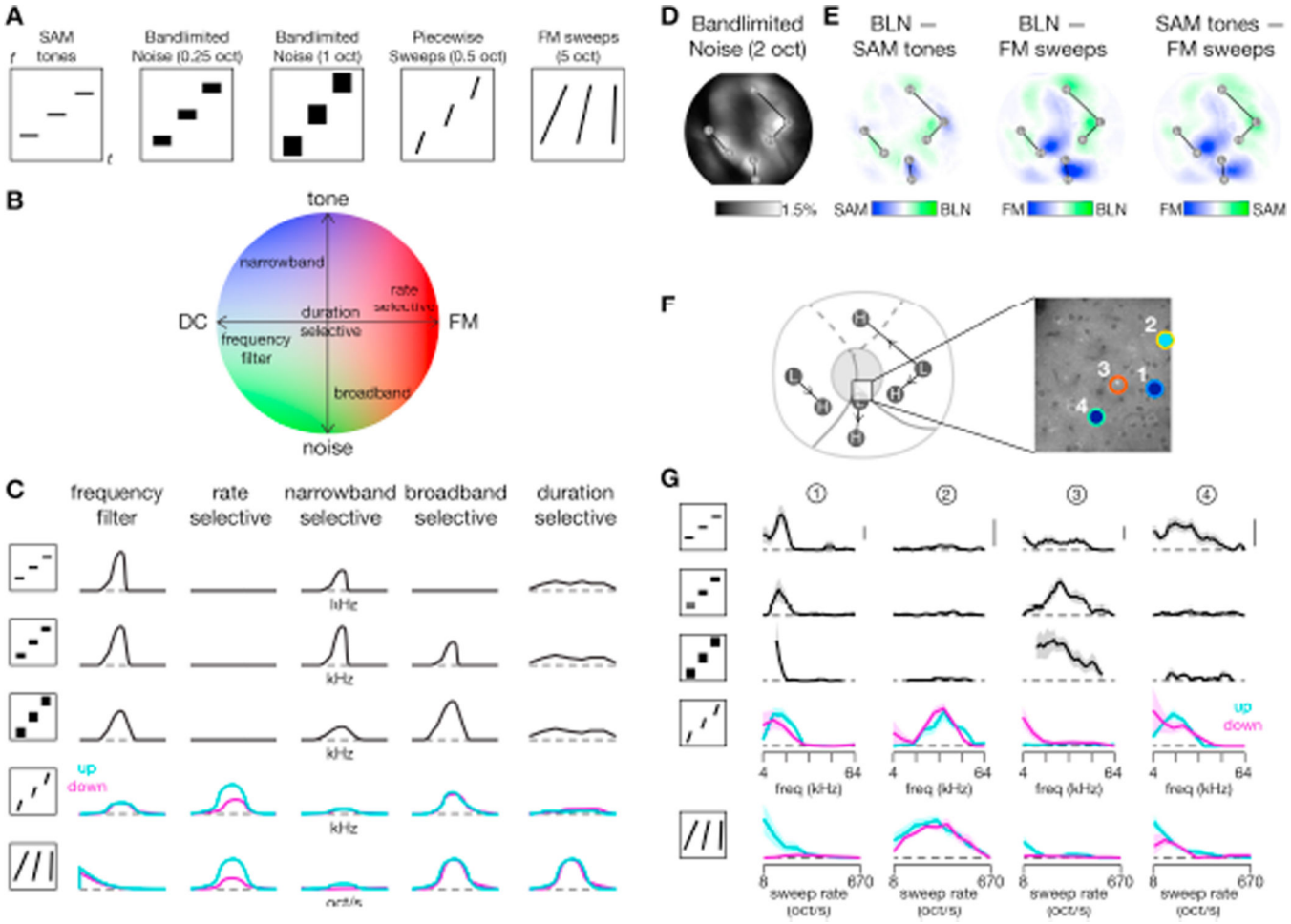

Figure 8. Differences in responses of individual neurons to bandlimited noise and piecewise sweeps

(A) Stylized spectrograms illustrate classes of stimuli used. Stimuli shown as black line or rectangle and each repeat indicates changes as the parameter of interest (frequency or sweep rate) is altered within a single stimulus set. Time *t* on *x*-axis and frequency *f* on *y*-axis.

(B) Hypothetical response space, where *x*-axis indicates whether a neuron responds to static DC components (left) or temporal dynamics (right) and *y*-axis indicates whether a neuron responds to pure tones (top) or broadband spectral energy (bottom). Colors indicate general stimulus preference: red for FM sweeps, blue for pure tones, and green for BLN.

(C) Predicted responses for neurons of each response type labeled in panel B to each of the stimulus classes shown in panel A.

(D) Average response seen under widefield imaging across a set of 10 noise bursts ranging in center frequency from 6 to 48 kHz. Each stimulus filtered by a 2-octave bandpass filter. Noise bursts were 300 msec with a 10 Hz envelope and presented at −20 dB attenuation. Same experiment as shown in Figure 2.

(E) Difference in responses between BLN, SAM tones, and FM sweeps on a pixel-by-pixel basis. Responses are most similar for BLN and SAM tones.

(F) Location of two-photon imaging field (left) and individual neurons (right) to be shown in panel D. Same format as Figure 5A. Different experiment from panels D-E.

(G) Tuning curves for four neurons in response to all stimulus classes. Each row is a tuning curve in response to the corresponding stimulus. BLN of 300 msec with 10 Hz envelope swept from 4 to 64 kHz with a 0.25 octave bandpass filter (second row) or from 6 to 48 kHz with a 1 octave bandwidth (third row). PWS swept from 4 to 64 kHz at 10 oct/s. Stimuli lasted 50 msec so that each stimulus covered 0.5 octaves. All stimuli at −40 dB attenuation. Vertical bar indicates 5 events/s. For PWS and FM sweeps, responses to upward and downward sweeps are shown as cyan and magenta curves, respectively. All curves smoothed with a 3-point moving average and ± SEM indicated by shaded regions.

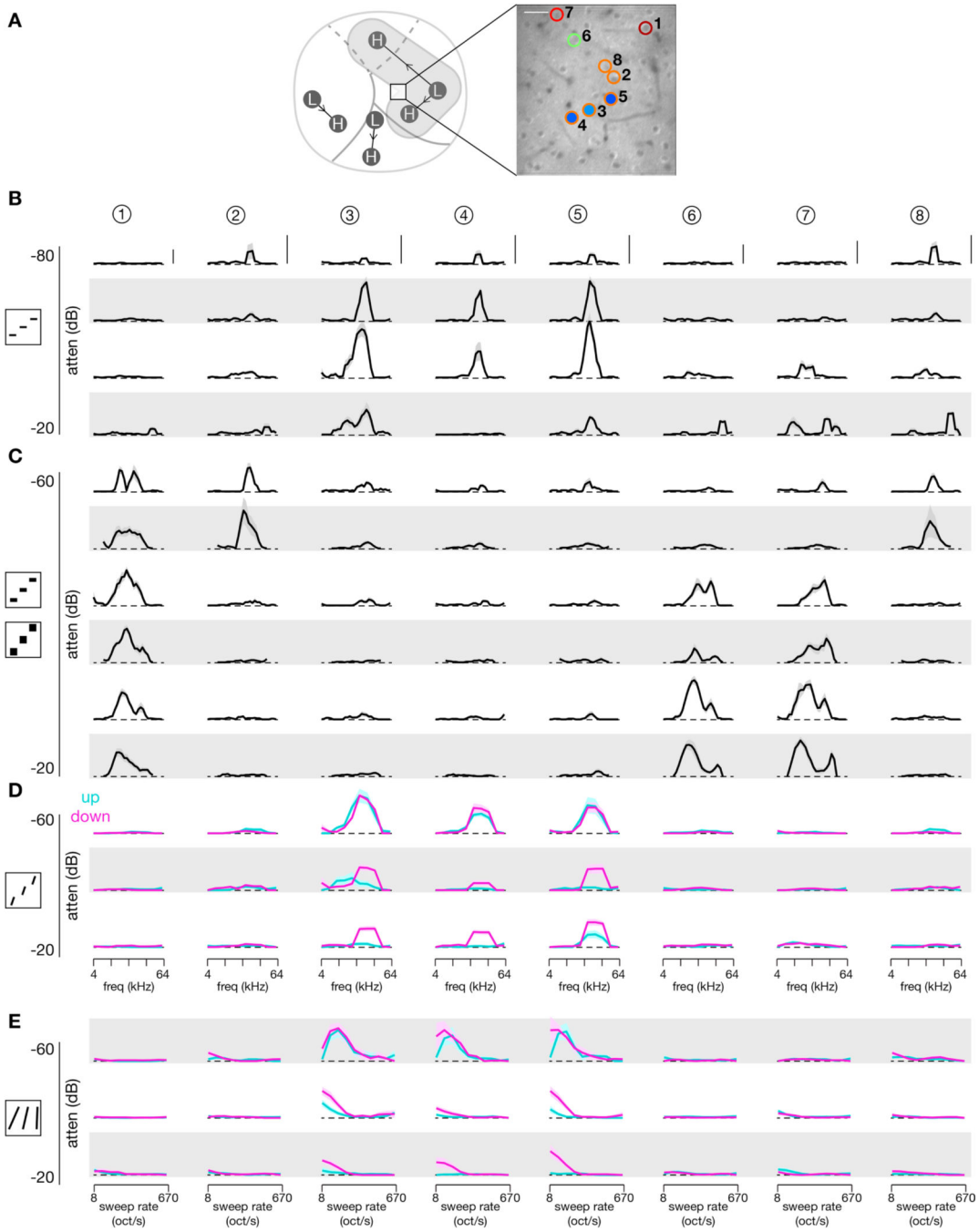

Figure 9. Tuning curves across stimuli for a local population of individual neurons

Comprehensive responses across a large array of stimuli for 8 neurons from a single two-photon imaging field. Means shown as dark trace and ± SEM as shaded region. For PWS and FM sweeps, responses to upward sweeps are shown in cyan and responses to downward sweeps in magenta. Scale bar: 10% $\Delta F/F_O$.

(A) Location of two-photon imaging field (left) and individual neurons (right).

(B) SAM tone tuning curves across four different sound levels.

(C) BLN tuning across three different sound levels and two different octave ranges. Top two rows show responses to 0.25-octave BLN stimuli (top) and 1-octave BLN stimuli (second row) at −60 dB attenuation. Next two rows show responses to 0.25-octave and 1-octave BLN stimuli at −40 dB attenuation, and final two rows show responses at −20 dB attenuation.
(D) PWS tuning across three different sound levels. Each stimulus swept at 10 oct/s for 0.5 s, resulting in a frequency span of 0.5 octaves. Ten different center frequencies and two different directions (up and down) were used.
(E) FM sweep tuning across three different sound levels. Each stimulus swept from 3 to 96 kHz with sweep rate and direction varied.

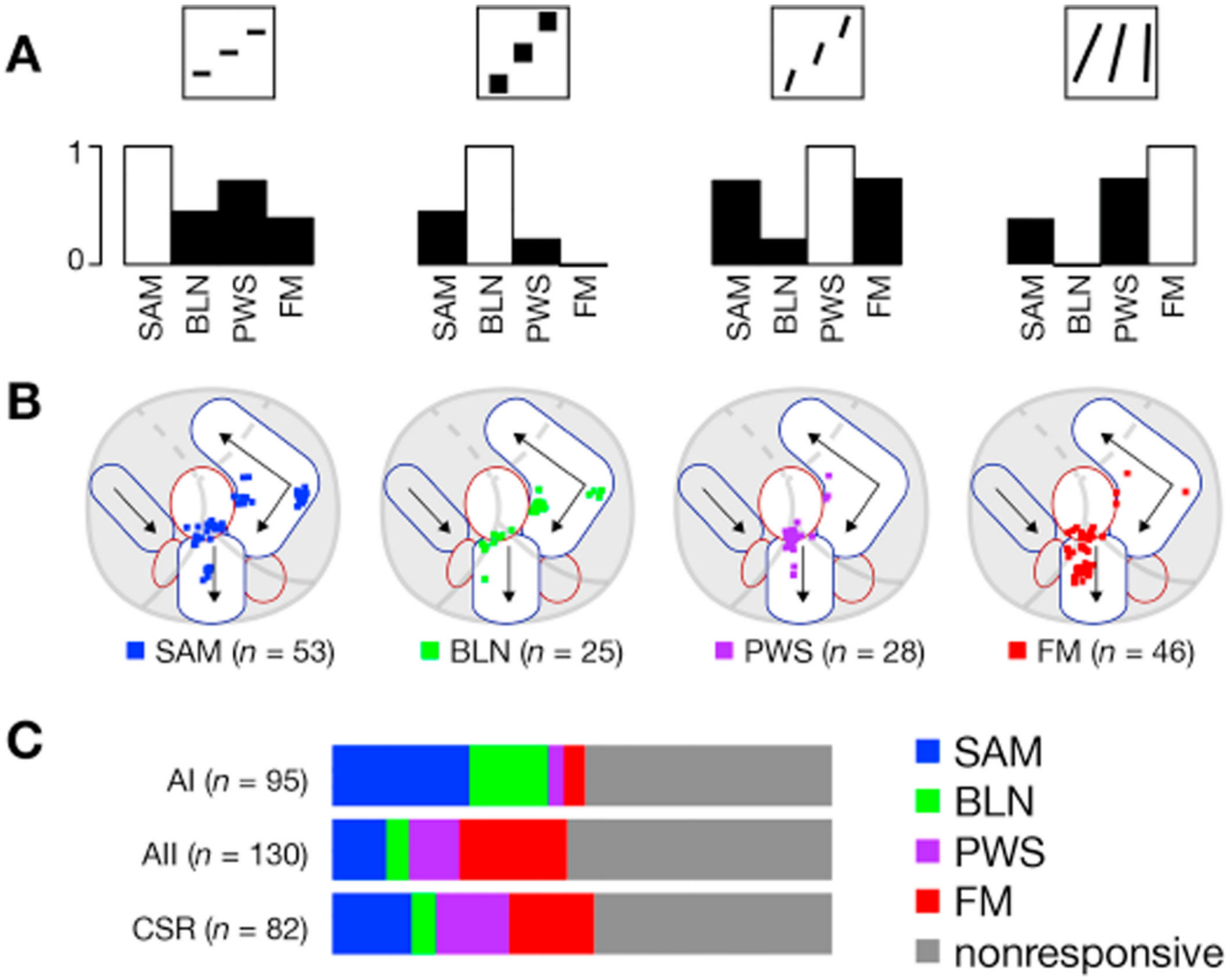

Figure 10. Neurons across different regions belong to different response classes

(A) Bar plots showing correlation between respective stimulus class (indicated by thumbnail in top row) and all the other stimulus classes for neurons responsive to at least one stimulus class. For reference, autocorrelation (equal to 1) shown as white bar.

(B) Neurons were categorized as SAM, BLN, PWS, or FM based on which stimulus drove the largest response in that neuron and plotted on a common coordinate system as in Figure 7. Only neurons responsive to at least one stimulus class are included.

(C) Relative distribution of neurons for each cortical region studied. Neurons are classified as in B (with nonresponsive neurons included as well) and bar plot is color-coded as indicated on right. The percentage of neurons that responded to each stimulus class was 25% for SAM tones, 19% for FM sweeps, 20% for BLN, and 24% for PWS; 152 neurons (or 49.5%) responded significantly to at least one class. For neuropil-subtracted data, the percentage of responsive neurons fell to 15% for SAM tones, 12% for FM sweeps, 12% for BLN, and 17% for PWS; 118 neurons (38.4%) responded to at least one class. Neurons were roughly equally distributed between AI (n = 95), AII (n = 130), and CSR (n = 82).

Table 1

Counts of neurons with tone, sweep, and direction selectivity

Active neurons were registered to each of the three fields based on location relative to low- and high-frequency landmarks from widefield imaging. Cells were assigned to each of the indicated categories based on presence of significant response to that stimulus. Included in the total are 20 neurons not located in any of the three fields. Largest category for each region denoted in bold. For direction selectivity, 2-way ANOVA was calculated for responses to FM sweeps with sweep rate and direction as the variables; $p < 0.1$ was used to determine a significant direction selectivity.

	# fields	# active neurons	# sound-responsive (%)	# tone only (%)	# tone + sweep (%)	# sweep only (%)	# direction selective (%)
			% of active	% of sound-responsive			% of sweep-responsive
AI	15	498	143 (29%)	**92 (64%)**	41 (29%)	10 (7%)	40 (78%)
AII	14	248	97 (39%)	33 (34%)	**36 (37%)**	28 (29%)	21 (33%)
CSR	8	154	71 (46%)	16 (23%)	11 (15%)	**44 (62%)**	24 (44%)
Total	32	920	318 (35%)	141 (44%)	89 (28%)	88 (28%)	87 (49%)